ONERA
THE FRENCH AEROSPACE LAB

Design and optimization of lattice structures for aerospace applications

Enrico Stragiotti

François-Xavier Irisarri[1], Cédric Julien[1] and Joseph Morlier[2]

1: ONERA - The French Aerospace Lab
DMAS - Département matériaux et structures
92320 Châtillon, France
{francois-xavier.irisarri, cedric.julien}@onera.fr

2: ICA - Institut Clément Ader
ISAE - SUPAERO
31400 Toulouse, France
joseph.morlier@isae-supaero.fr

October 17, 2023

PhD manuscript

ONERA – ISAE Supaero

Colophon

This document was typeset with the help of KOMA-Script and LaTeX using the kaobook class.

ONERA – ISAE Supaero

Contents

List of Figures

List of Tables

List of Abbreviations

DOFs	Degrees Of Freedom
HS	Hashin-Shtrikman
KS	Kreisselmeier-Steinhauser
LP	Linear Programming
MMA	Method of Moving Asymptotes
MPVCs	Mathematical Programs with Vanishing Constraints
NAND	Nested Analysis and Design
NLP	Non-Linear Programming
SAND	Simultaneous Analysis and Design
SIMP	Solid Isotropic Material with Penalization Method
SLP	Sequential Linear Programming
TTO	Truss Topology Optimization

Evaluating discretization approaches for ultralight structure optimization

1

The process of topology optimization for a structure involves the selection and sizing of optimal elements within a predetermined set. As discussed in the previous chapter, in our context this set could be composed of either continuum elements (shell or volumetric) or truss-like elements. This chapter aims to assess the suitability and the inherent advantages and disadvantages of both methodologies when optimizing ultralight structures i.e. structures that exhibit an extremely low volume fraction, typically below 1%.

For this purpose, we initially establish a common optimization formulation in Section 1.1. The classic compliance minimization with volume constraint problem is reformulated as a volume minimization problem with maximum stress constraints for both discretizations. Later, this framework is applied to optimize a two-dimensional test case, featuring identical dimensions, loads, and material properties. The outcomes of the comparison of both discretization approaches are presented and discussed in Section 1.2.

Part of the content presented in this chapter has been published and showcased during a conference as: Stragiotti, E. et al. (2021) "Towards manufactured lattice structures: a comparison between layout and topology optimization", in *AeroBest 2021 International Conference on Multidisciplinary Design Optimization of Aerospace Systems*. Book of proceedings. Lisbon, Portugal: ECCOMAS [1].

1.1 The formulation of a common problem: volume minimization with stress constraints

Two of the most frequently employed formulations for structural optimization are the minimization of volume while adhering to stress constraints and the minimization of compliance under volume constraints. Historically, the volume minimization formulation has been used in the first works of structural optimization of truss structures [2–4]. The problem was initially formulated in terms of member forces, ignoring the kinematic compatibility to obtain a Linear Programming (LP) problem. The formulation was modeled using the Simultaneous Analysis and Design (SAND) approach, where the equations of nodal equilibrium are treated as equality constraints, and where both nodal displacements and the cross-sectional areas of truss members serve as design variables [5].

However, to attain greater design freedom, the structure optimization field later transitioned from truss structures to continuous discretization. While truss structures offered simplicity and ease of analysis, they imposed limitations on design due to their discrete member configurations. The continuum mesh offered instead more versatility [6, 7], and has since been used for multiple different applications, e.g. the design of metamaterials [8, 9] or the simulation of advanced manufacturing constaints [10, 11]. The SAND approach is incompatible with continuum meshes due to its excessive number of variables[1].

2. Dorn et al. (1964), 'Automatic design of optimal structures'
3. Chan (1964), 'Optimum structural design and linear programming'
4. Hemp (1973), 'Optimum Structures'
5. Sankaranarayanan et al. (1994), 'Truss topology optimization with simultaneous analysis and design'
6. Bendsøe et al. (1988), 'Generating optimal topologies in structural design using a homogenization method'
7. Bendsøe (1989), 'Optimal shape design as a material distribution problem'
8. Sigmund (1994), 'Materials with prescribed constitutive parameters'
9. Zhang et al. (2006), 'Scale-related topology optimization of cellular materials and structures'
10. Sigmund (2009), 'Manufacturing tolerant topology optimization'
11. Brackett et al. (2011), 'Topology Optimization for Additive Manufacturing'

1: This preposition holds when referring to the end of the 1980s when computational power was scarce compared to what we have today.

Given this limitation, a new approach was required to better handle the complexity of continuum meshes.

In the Nested Analysis and Design (NAND) approach, the nodal displacement (state) variables are eliminated from the optimization problem through a process where the structural equilibrium equation is solved every iteration instead of being used as a constraint of the optimization. This results in an independent nested phase where the state equation of structural equilibrium is solved separately from the optimization algorithm. This creates a dense coupling between displacement and material density variables, necessitating a computationally expensive sensitivity analysis within the nested algorithm, typically employing the adjoint method (more information about the adjoint method on the following resurces [12, 13]). Nevertheless, if the problem is reformulated as a compliance minimization with volume constraints, the problem is self-adjoint and the adjoint algorithm is no longer necessary to evaluate the gradient sensitivities [14].

12. Tortorelli et al. (1994), 'Design sensitivity analysis'
13. Martins et al. (2021), 'Engineering Design Optimization'
14. Bendsøe et al. (2004), 'Topology Optimization'

However, our emphasis on operating within the aerospace sector aligns more favorably with the volume minimization problem. The choice to prioritize volume minimization in the aerospace sector is underpinned by a range of economic, environmental, and performance-related factors. It is a strategic approach that aligns with industry goals of sustainability, efficiency, and technological advancement. Additionally, as we will see later in this thesis, the volume minimization formulation will permit adding local buckling and maximum displacement constraints more easily. We have opted, thus, to employ the volume minimization optimization formulation for our study, and we will now review how this formulation is implemented on continuum and truss-like meshes.

1.1.1 Continuous discretization NAND minimum volume formulation

This section introduces the NAND volume minimization formulation of topology optimization for continuum meshes. We will start however presenting the more common minimum compliance formulation to explain the important notations and concepts that will be essential in developing the volume minimization formulation.

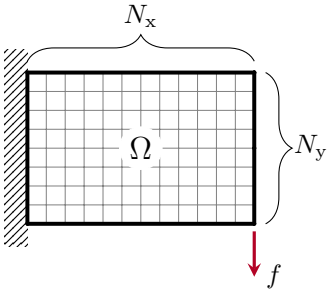

Figure 1.1: The domain Ω is discretized using $N_e = N_x N_y$ continuous 4-nodes elements.

Minimum compliance formulation Let $\Omega \in \mathbb{R}^2$ be a rectangular domain in of dimensions X and Y, containing respectively N_x and N_y linear 4-nodes elements, for a total of $N_e = N_x N_y$ elements and M nodes (see Fig. 1.1). The objective of the optimization is the minimization of the compliance C of the structure, equivalent to finding the structure with the least possible nodal displacement with respect to a defined set of boundary conditions. The Problem $\mathbb{T}_0$ is

stated in terms of the design variables $\boldsymbol{\rho}$ as follows:

$$\begin{aligned} \min_{\boldsymbol{\rho}} \quad & C = \sum_i \boldsymbol{u}_{e,i}^T \boldsymbol{K}_{e,i} \boldsymbol{u}_{e,i} = \boldsymbol{f}^T \boldsymbol{u} && \forall i \in [0, \dots, N_\mathrm{e}] \\ \text{s.t.} \quad & \frac{\sum_i \left(\overline{\widetilde{\rho}}_i v_i\right) / V_0}{V_\mathrm{p}} - 1 \leq 0 && \forall i \in [0, \dots, N_\mathrm{e}] \qquad (\mathbb{T}_0) \\ & \boldsymbol{K}\boldsymbol{u} = \boldsymbol{f} \\ & 0 \leq \rho_i \leq 1. && \forall i \in [0, \dots, N_\mathrm{e}] \end{aligned}$$

The design variables $\boldsymbol{\rho}$ are defined for every element of the structure as $\boldsymbol{\rho} = [\rho_1, \rho_2, \dots, \rho_{Ne}]^T$, with $\rho_i \in [0, 1],\ \forall i \in [0, \dots, N_\mathrm{e}]$. The physical densities $\overline{\widetilde{\boldsymbol{\rho}}}$ are related to design variables through density filtering and threshold projection [15], as explained later in the document. V_p is the prescribed volume fraction that acts as the constraint of the minimization problem, while v_i represents the area of the i-th element and V_0 is the total area of the domain Ω. $\boldsymbol{K}\boldsymbol{u} = \boldsymbol{f}$ is the state equation of the problem and defines the elastic response of the structure to an external nodal load $\boldsymbol{f} = [f_1, f_2, \dots, f_{2M}]^T$. The global stiffness matrix $\boldsymbol{K}$ is assembled from the element stiffness matrix $\boldsymbol{K} = \sum_{i \in \Omega} \boldsymbol{K}_{e,i}$ and $\boldsymbol{K}_{e,i} = E_i \boldsymbol{K}_{e,0}$ where $\boldsymbol{K}_{e,0}$ represents the element stiffness matrix relative to the chosen type of element (linear or quadratic) and $E_i(\overline{\widetilde{\rho}}_i)$ the Young's modulus of the i-th element.

15. Wang et al. (2011), 'On projection methods, convergence and robust formulations in topology optimization'

The material scheme used to interpolate between void and full material is the well-known Solid Isotropic Material with Penalization Method (SIMP) [7, 16] approach. It is governed by the equation:

$$E_i(\overline{\widetilde{\rho}}_i) = E_{\min} + \overline{\widetilde{\rho}}_i^{\,p} (E_0 - E_{\min}), \tag{1.1}$$

7. Bendsøe (1989), 'Optimal shape design as a material distribution problem'

16. Bendsøe et al. (1999), 'Material interpolation schemes in topology optimization'

where the parameter p penalizes the intermediate densities and pushes the result to a black-and-white result. E_0 is the Young's modulus of the dense material and $E_{\min}$ is a small value used to avoid the global stiffness matrix $\boldsymbol{K}$ from being singular when $\overline{\widetilde{\rho}}_i = 0$.

In this study we set these parameters to $E_0 = 1$, and $E_{\min} = 10^{-9}$. The value of the penalization parameter p is selected as $p = 3$ because in that way the intermediate densities respect the Hashin-Shtrikman (HS) bounds [16, 17]. These relationships describe the boundaries of attainable isotropic material characteristics when dealing with composites (materials with microscopic structures) using two specified, linearly elastic, isotropic materials (in our case the solid and the empty phases).

17. Hashin et al. (1963), 'A variational approach to the theory of the elastic behaviour of multiphase materials'

Spatial filtering and projection Multiple approaches have been developed to solve the problems linked to mesh discretization, such as mesh dependence or the checkerboard problem [18]. Filtering the sensitivity information of the optimization problem proved to

18. Díaz et al. (1995), 'Checkerboard patterns in layout optimization'

be an effective approach to guarantee independence from mesh resolution [19, 20]. In the present research, we decided instead to directly filter the density field $\boldsymbol{\rho}$ using the 2D convolution operator [21]. The weight function w (or kernel) of the convolution is defined as:

$$w(d_j) = R - d_j, \quad j \in \mathbb{N}_{i,R} \tag{1.2}$$

where $\mathbb{N}_{i,R}$ represent the set of elements lying within a circle of radius R centered on the i-th element and d_j is the distance of the j-th element to the center of the filter (see Fig. 1.2).

19. Sigmund (1994), 'Design of Material Structures using Topology Optimization'

20. Sigmund (1997), 'On the Design of Compliant Mechanisms Using Topology Optimization'

21. Sigmund (2007), 'Morphology-based black and white filters for topology optimization'

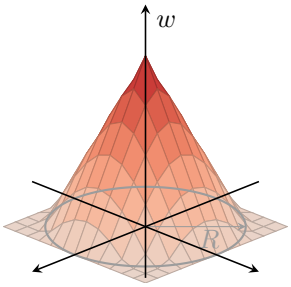

Figure 1.2: Kernel of the 2D convolution operator.

The filtered values of the design variable are calculated as:

$$\widetilde{\rho}_i = \frac{\sum_{j\in\mathbb{N}_{i,R}} w(d_j)v_j\rho_j}{\sum_{j\in\mathbb{N}_{i,R}} w(d_j)v_j}. \tag{1.3}$$

As the filtering phase produces a large number of gray elements, a smooth projection technique based on the *tanh* function is implemented [15]:

$$\overline{\widetilde{\rho}}_j = \frac{\tanh(\beta\eta) + \tanh(\beta(\widetilde{\rho}_j - \eta))}{\tanh(\beta\eta) + \tanh(\beta(1-\eta))}, \tag{1.4}$$

where β is a parameter that defines the slope of this approximation function: the larger the value of β, the less intermediate elements are present in the structure topology. η is the threshold value of the projection. Using Equation 1.4 is not volume conservative for all values of η, and to stay conservative we use a volume-increasing filter [22]. The value of $\eta = 0.4$ is then chosen.

15. Wang et al. (2011), 'On projection methods, convergence and robust formulations in topology optimization'

22. Ferrari et al. (2020), 'A new generation 99 line Matlab code for compliance topology optimization and its extension to 3D'

The derivative of the filtered density $\widetilde{\boldsymbol{\rho}}$ with respect to the design variable $\boldsymbol{\rho}$ is written deriving Equation 1.3:

$$\frac{\partial\widetilde{\rho}_i}{\partial\rho_j} = \frac{w(d_j)v_j}{\sum_{j\in\mathbb{N}_{i,R}} w(d_j)v_j}. \tag{1.5}$$

The sensitivity of the physical densities $\overline{\widetilde{\boldsymbol{\rho}}}$ with respect to the filtered $\widetilde{\boldsymbol{\rho}}$ can be written as:

$$\frac{\partial\overline{\widetilde{\rho}}_j}{\partial\widetilde{\rho}_j} = \beta\frac{1-\tanh^2(\beta(\widetilde{\rho}_j-\eta))}{\tanh(\beta\eta)+\tanh(\beta(1-\eta))}. \tag{1.6}$$

Using the chain rule it is possible to write:

$$\frac{\partial h}{\partial\rho_i} = \sum_{j\in\mathbb{N}_{i,R}} \frac{\partial f}{\partial\overline{\widetilde{\rho}}_j}\frac{\partial\overline{\widetilde{\rho}}_j}{\partial\widetilde{\rho}_j}\frac{\partial\widetilde{\rho}_j}{\partial\rho_i}, \tag{1.7}$$

where h represents a generic function.

Objective and constraint functions Up until this point, we have been focused on the compliance minimization formulation $\mathbb{T}_0$. Moving forward, we introduce the necessary modifications to transition into the volume minimization formulation with stress constraints. This formulation will be used to compare the continuous mesh with truss-like structure optimization.

The objective of the optimization is to minimize the volume of a structure subject to a specified load case. The volume of the structure V is expressed as a fraction of the total volume V_0 of the domain Ω:

$$V = \frac{1}{V_0} \sum_{i \in \Omega} \overline{\widetilde{\rho}}_i v_i. \tag{1.8}$$

In this thesis, we assume that the elementary volume occupied by the i-th element v_i is equal for all the elements, and thus Equation 1.8 is simplified as follows:

$$V = \frac{1}{N_e} \sum_{i \in \Omega} \overline{\widetilde{\rho}}_i. \tag{1.9}$$

The normalized local stress constraint $\boldsymbol{g}_{\text{st}}$ are formulated as:

$$\frac{\sigma_{\text{VM},j}}{\sigma_L} - 1 \leq 0, \quad \forall j \in \Omega_{mat}(\boldsymbol{\rho}) \tag{g_{st}}$$

where $\Omega_{mat}(\boldsymbol{\rho}) \subseteq \Omega$ represents the design-dependent set of elements with a non-zero density, $\sigma_{\text{VM},j}$ is the equivalent Von Mises stress for the j-th element, and σ_L is the maximum allowable of the material.

The first difficulty that arises is that the stress constraints are defined only for the elements where $\overline{\widetilde{\rho}}_i > 0$, while $\overline{\widetilde{\rho}}_i \in [0, 1]$. Thus, the set of constraints changes during the optimization. This class of problems is called Mathematical Programs with Vanishing Constraints (MPVCs) [23] and is known for being difficult to solve with a gradient descent optimization algorithm. The original set of constraints $\boldsymbol{g}_{\text{st}}$ is then reformulated into an equivalent design-independent set of constraints $\bar{\boldsymbol{g}}_{\text{st}}$ as follows [24]:

23. Achtziger et al. (2008), 'Mathematical programs with vanishing constraints'

24. Cheng et al. (1992), 'Study on Topology Optimization with Stress Constraints'

$$\overline{\widetilde{\rho}}_i \left(\frac{\sigma_{\text{VM},i}}{\sigma_L} - 1 \right) \leq 0, \quad \forall i \in \Omega. \tag{$\bar{g}_{\text{st}}$}$$

Von Mises stress evaluation The evaluation of the equivalent stress of an element follows the formulation proposed by Von Mises. Let us take a four-node quadrilateral linear element with a single integration (or Gauss) point in the center and four $2a$ equal-length sides (see Fig. 1.3). If bilinear shape functions are used to interpolate the displacement field, we can evaluate the deformations at the

integration point as:

$$\begin{pmatrix}\varepsilon_x\\ \varepsilon_y\\ \gamma_{xy}\end{pmatrix} = \boldsymbol{B}_s\boldsymbol{q}_s, \text{ with } \boldsymbol{B}_s = \frac{1}{4a}\begin{pmatrix}-1 & 1 & 1 & -1 & 0 & 0 & 0 & 0\\ 0 & 0 & 0 & 0 & -1 & -1 & 1 & 1\\ -1 & -1 & 1 & 1 & -1 & 1 & 1 & -1\end{pmatrix}, \tag{1.10}$$

where $\boldsymbol{q}_s = (u_1, u_2, u_3, u_4, v_1, v_2, v_3, v_4)^T$ represents the vector of the displacement degrees of freedom of the element.

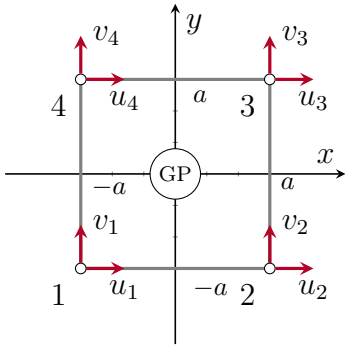

Figure 1.3: A four-node quadrilateral element. GP is the Gaussian integration point for which the equivalent stress is evaluated.

The stress tensor is evaluated using the elasticity Hooke's law in 2D as follows:

$$\begin{pmatrix}\sigma_x\\ \sigma_y\\ \tau_{xy}\end{pmatrix} = \boldsymbol{C}_e\begin{pmatrix}\varepsilon_x\\ \varepsilon_y\\ \gamma_{xy}\end{pmatrix} \quad \text{with} \quad \boldsymbol{C}_e = \frac{E}{1-\nu^2}\begin{pmatrix}1 & \nu & 0\\ \nu & 1 & 0\\ 0 & 0 & G\end{pmatrix}. \tag{1.11}$$

The equivalent Von Mises stress of the element can then be written as:

$$\langle\boldsymbol{\sigma}_{\text{VM}}\rangle = \sqrt{\sigma_x^2 + \sigma_y^2 - \sigma_x\sigma_y + 3\tau_{xy}} \tag{1.12}$$

$$= \sqrt{\begin{pmatrix}\sigma_x & \sigma_y & \tau_{xy}\end{pmatrix}\begin{pmatrix}1 & -1/2 & 0\\ -1/2 & 1 & 0\\ 0 & 0 & 3\end{pmatrix}\begin{pmatrix}\sigma_x\\ \sigma_y\\ \tau_{xy}\end{pmatrix}} \tag{1.13}$$

$$= \sqrt{\boldsymbol{q}_s^T\boldsymbol{B}_s^T\boldsymbol{C}_e^T\boldsymbol{D}_{\text{VM}}\boldsymbol{C}_e\boldsymbol{B}_s\boldsymbol{q}_s}, \text{ with } \boldsymbol{D}_{\text{VM}} = \begin{pmatrix}1 & -1/2 & 0\\ -1/2 & 1 & 0\\ 0 & 0 & 3\end{pmatrix} \tag{1.14}$$

$$\langle\boldsymbol{\sigma}_{\text{VM}}\rangle = \sqrt{\boldsymbol{q}_s^T\boldsymbol{S}\boldsymbol{q}_s}, \quad \text{with } \boldsymbol{S} = \boldsymbol{B}_s^T\boldsymbol{C}_e^T\boldsymbol{D}_{\text{VM}}\boldsymbol{C}_e\boldsymbol{B}_s. \tag{1.15}$$

Microscopic and macroscopic stress In stress-constrained topology optimization, the element stress is usually evaluated using the microscopic stress formulation, assuming that there is no direct correlation between stress and density [25]. Indeed, the use of the macroscopic stress in volume minimization optimization problems creates an all-void design [26]. The properties that the microscopic stress should present are:

(i) The stress criterion should be mathematically as simple as possible, as the relationship between Young's modulus and density. This permits a simple numerical implementation.
(ii) To mimic the real physical behavior, the microscopic stress should be inversely proportional to density.
(iii) The microscopic stress should converge to a non-zero value at zero density. This requisite is deduced from investigations into the asymptotic stress behavior in thin layers [27].

25. Duysinx et al. (1998), 'Topology optimization of continuum structures with local stress constraints'
26. Le et al. (2010), 'Stress-based topology optimization for continua'
27. Verbart et al. (2017), 'A unified aggregation and relaxation approach for stress-constrained topology optimization'

The relation between stress and displacement is written as:

$$\langle \sigma_{\text{VM}} \rangle = \boldsymbol{C}_e(\langle E \rangle)\langle \boldsymbol{\varepsilon} \rangle, \tag{1.16}$$

where the variables between angular brackets $\langle \dots \rangle$ represent macroscopic variables.

Combining (i) and (ii) with Equations 1.1, and 1.16, the microscopic stress can be written as:

$$\sigma_{\text{VM}} = \frac{\langle \sigma_{\text{VM}} \rangle}{\rho_e^q} = \rho_e^{p-q} \boldsymbol{C}_e(E_0)\langle \boldsymbol{\varepsilon} \rangle, \tag{1.17}$$

where the exponent q is a number greater than 1.

One possible choice that satisfy all the requirements is $q = p$ [26–29]. Thus, the microscopic stress is defined as:

$$\sigma_{\text{VM}} = \boldsymbol{C}_e(E_0)\langle \boldsymbol{\varepsilon} \rangle. \tag{1.18}$$

From a physical perspective, the significance of microscopic stress becomes evident when considering an element with intermediate density and a porous microstructure. The microscopic stress presented in Equation 1.18 measures the stress of the microstructure. It is grounded in the assumption that the macroscopic deformations of the homogenized element generate within the microstructure of the element a stress state that remains unaffected by the density of the element itself.

26. Le et al. (2010), 'Stress-based topology optimization for continua'
27. Verbart et al. (2017), 'A unified aggregation and relaxation approach for stress-constrained topology optimization'
28. Holmberg et al. (2013), 'Stress constrained topology optimization'
29. Silva et al. (2019), 'Stress-constrained topology optimization considering uniform manufacturing uncertainties'

Constraints aggregation and relaxation When optimizing a structure with stress constraints using a NAND formulation, two primary challenges commonly arise:

(i) Is it known in the literature [30, 31] that stress-based topology optimization suffers from the *singular minima* (or *singularity*) problem: firstly observed on truss structure optimization [32], these *minima* are almost inaccessible to a standard gradient-based optimizer, and they represent the *minima* of the optimization. This is because achieving the optimal solution to a problem using continuous design variables may necessitate passing through a state where the optimization constraints are violated, i.e. the *minimum* is on a lower dimension compared to the design space. This problem is often solved using a technique called *constraints relaxation* [33].

(ii) The stress is a local measure, and thus a large set of constraints is generated when a reasonably fine mesh is used (one element, one constraint). This problem is often solved using a technique called *constraints aggregation* or *global constraints* [34].

Following the work developed by Verbart *et al.* [27], the lower bound

33. Cheng et al. (1997), 'ε-relaxed approach in structural topology optimization'
34. Silva et al. (2021), 'Local versus global stress constraint strategies in topology optimization'
27. Verbart et al. (2017), 'A unified aggregation and relaxation approach for stress-constrained topology optimization'

35. Kreisselmeier et al. (1979), 'Systematic Control Design by Optimizing a Vector Performance Index'

Kreisselmeier-Steinhauser (KS) function [35] is used to approximate the local relaxed stress constraint maximum. The authors discovered that employing lower-bound KS aggregation functions to approximate the maximum operator in stress-constrained topology optimization eliminates the need for stress constraint relaxation methods to address the singularity issue. This is because the lower-bound functions inherently offer a combined effect of constraint aggregation and relaxation. The KS aggregated stress constraint function is defined as follows:

$$G_{\mathrm{KS}}^{\mathrm{L}} = \frac{1}{P} \ln\left(\frac{1}{N_{\mathrm{e}}} \sum e^{P\bar{g}_i}\right). \tag{1.19}$$

Its main advantage over other different formulations is that it uses a single hyperparameter P to control the aggregation and the relaxation of the constraints simultaneously.

Minimum volume formulation The NAND minimum volume formulation for continuous discretization is written combining Equations 1.9, and 1.19 as:

$$\begin{aligned} \min_{\rho} \quad & V = \frac{1}{N_e} \sum_{i \in \Omega} \overline{\widetilde{\rho}}_i, \\ \text{s.t.} \quad & G_{\mathrm{KS}}^{\mathrm{L}} = \frac{1}{P} \ln\left(\frac{1}{N_{\mathrm{e}}} \sum_{i \in \Omega} e^{P\bar{g}_i}\right) \leq 0 \\ & \boldsymbol{K}\boldsymbol{u} = \boldsymbol{F} \\ & 0 \leq \rho_i \leq 1, \end{aligned} \tag{$\mathbb{T}_1$}$$

The optimization is carried out using a gradient descent optimization algorithm for which the sensitivities are given in analytical form. Using analytic gradients is in general more efficient than finite differences as it avoids the need for multiple function evaluations, making the optimization process faster and more precise.

Sensitivity analysis of the objective function The objective of this section is to quickly present the calculation of the analytical sensitivity of the volume with respect to the design variable ρ. Deriving Equation 1.9 we obtain:

$$\frac{\partial V}{\partial \overline{\widetilde{\rho}}_i} = \frac{1}{N_e}. \tag{1.20}$$

The sensitivity of the objective function can then be evaluated using Equations 1.20, 1.5, 1.6, and 1.7 as follows:

$$\frac{dV}{d\rho_i} = \sum_{j \in \mathbb{N}_{i,R}} \frac{\partial V}{\partial \overline{\widetilde{\rho}}_j} \frac{\partial \overline{\widetilde{\rho}}_j}{\partial \widetilde{\rho}_j} \frac{\partial \widetilde{\rho}_j}{\partial \rho_i}. \tag{1.21}$$

Sensitivity analysis of the constraint function This section focuses on the details of the calculation of how the constraint function $G_{\mathrm{KS}}^{\mathrm{L}}$ changes with respect to the design variable $\boldsymbol{\rho}$.

As the constraint function $G_{\mathrm{KS}}^{\mathrm{L}} = G(\overline{\overline{\boldsymbol{\rho}}}, \boldsymbol{u}(\overline{\overline{\boldsymbol{\rho}}}))$ is explicitly and implicitly (via the relationship with $\boldsymbol{u}$) depending on $\overline{\overline{\boldsymbol{\rho}}}$, the first-order derivative is evaluated using the total derivative formula:

$$\frac{\partial G_{\mathrm{KS}}^{\mathrm{L}}}{\partial \overline{\overline{\rho}}_j} = \frac{dG}{d\overline{\overline{\rho}}_j} = \frac{\partial G}{\partial \overline{\overline{\rho}}_j} + \frac{\partial G}{\partial \boldsymbol{u}} \frac{d\boldsymbol{u}}{d\overline{\overline{\rho}}_j}. \tag{1.22}$$

As function $G_{\mathrm{KS}}^{\mathrm{L}}$ depends on $\boldsymbol{u}$ via the stresses σ_i, it is possible to write:

$$\frac{\partial G}{\partial \boldsymbol{u}} = \sum_{i \in \Omega} \left(\frac{\partial G}{\partial \sigma_i} \frac{\partial \sigma_i}{\partial \boldsymbol{u}} \right). \tag{1.23}$$

Combining Eq. 1.22 with Eq. 1.23, we obtain:

$$\frac{dG}{d\overline{\overline{\rho}}_j} = \underbrace{\frac{\partial G}{\partial \overline{\overline{\rho}}_j}}_{A} + \sum_{i \in \Omega} \left(\underbrace{\frac{\partial G}{\partial \sigma_i}}_{B} \underbrace{\frac{\partial \sigma_i}{\partial \boldsymbol{u}}}_{C} \right) \underbrace{\frac{d\boldsymbol{u}}{d\overline{\overline{\rho}}_j}}_{D}. \tag{1.24}$$

We compute the four factors separately:

A – The first term represents the explicit relationship of G to the physical densities and its calculation is straightforward:

$$\frac{\partial G}{\partial \overline{\overline{\rho}}_j} = \frac{1}{P} \frac{\left(\frac{\sigma_{\mathrm{VM},j}}{\sigma_L} - 1 \right) \frac{1}{N_{\mathrm{e}}} P e^{P \bar{g}_j}}{\frac{1}{N_{\mathrm{e}}} \sum_k e^{P \bar{g}_k}} = \left(\frac{\sigma_{\mathrm{VM},j}}{\sigma_L} - 1 \right) \frac{e^{P \bar{g}_j}}{\sum_k e^{P \bar{g}_k}}. \tag{1.25}$$

B – The second term can be calculated using the chain rule:

$$\frac{\partial G}{\partial \sigma_i} = \frac{\partial G}{\partial \bar{g}_i} \frac{\partial \bar{g}_i}{\partial \sigma_i} = \frac{1}{P} \frac{\frac{1}{N_{\mathrm{e}}} P e^{P \bar{g}_i}}{\frac{1}{N_{\mathrm{e}}} \sum_k e^{P \bar{g}_k}} \frac{\overline{\overline{\rho}}_i}{\sigma_L} = \frac{\overline{\overline{\rho}}_i}{\sigma_L} \frac{e^{P \bar{g}_i}}{\sum_k e^{P \bar{g}_k}}. \tag{1.26}$$

C – We reformulate Equation 1.15 to be written in global coordinates instead of local:

$$\sigma_i^2 = \boldsymbol{q}_s^T \boldsymbol{S} \boldsymbol{q}_s = \boldsymbol{u}^T |\boldsymbol{S_i}|_g \boldsymbol{u}, \tag{1.27}$$

where $|\boldsymbol{S_i}|_g$ represents the matrix $\boldsymbol{S}$ of Equation 1.15written on global coordinates [2]. We can now differentiate Equation 1.27 with respect of the displacement field in global coordinates $\boldsymbol{u}$ to obtain:

$$\frac{\partial \sigma_i}{\partial \boldsymbol{u}} = \frac{|\boldsymbol{S_i}|_g \boldsymbol{u}}{\sigma_i}. \tag{1.28}$$

Equations 1.26, and 1.28 are now combined to obtain the result

2: The matrix $|\boldsymbol{S_i}|_g$ can be calculated using the very same assembling approach used for the stiffness matrix $\boldsymbol{K}$ starting from the elemental stiffness matrix $\boldsymbol{K}_e$. As the global stiffness matrix $\boldsymbol{K}$, $|\boldsymbol{S_i}|_g$ is symmetric and sparse.

of the product of the **B** and **C** terms. As a result, the derivatives of G with respect to $\boldsymbol{u}$, are written as:

$$\frac{\partial G}{\partial \boldsymbol{u}} = \frac{\frac{\bar{\bar{\rho}}_j}{\sigma_L \sigma_j} e^{P\bar{g}_i}}{\sum_i e^{P\bar{g}_i}} |\boldsymbol{S_j}|_g \boldsymbol{u}. \tag{1.29}$$

D – To calculate the last term, we take the static equilibrium equation $\boldsymbol{K}\boldsymbol{u} = \boldsymbol{f}$ and differentiate it with respect to the physical densities $\bar{\bar{\rho}}_j$, obtaining:

$$\frac{\partial \boldsymbol{K}}{\partial \bar{\bar{\rho}}_j}\boldsymbol{u} + \boldsymbol{K}\frac{\partial \boldsymbol{u}}{\partial \bar{\bar{\rho}}_j} = 0 \iff \frac{\partial \boldsymbol{u}}{\partial \bar{\bar{\rho}}_j} = -\boldsymbol{K}^{-1}\frac{\partial \boldsymbol{K}}{\partial \bar{\bar{\rho}}_j}\boldsymbol{u}, \tag{1.30}$$

where

$$\frac{\partial \boldsymbol{K}}{\partial \bar{\bar{\rho}}_j} = (E_0 - E_{\min}) p \bar{\bar{\rho}}_j^{p-1} \boldsymbol{K}_{e,j}. \tag{1.31}$$

Equation 1.31 represent the well-known first-derivative term of the global stiffness matrix $\boldsymbol{K}$ with respect to the physical densities $\bar{\bar{\rho}}_j$ when using SIMP material scheme [14]. We finally obtain the last term:

14. Bendsøe et al. (2004), 'Topology Optimization'

$$\frac{d\boldsymbol{u}}{d\bar{\bar{\rho}}_j} = -\boldsymbol{K}^{-1}\left((E_0 - E_{\min}) p \bar{\bar{\rho}}_j^{p-1} \boldsymbol{K}_e\right)\boldsymbol{u}. \tag{1.32}$$

Combining Eq. 1.24, Eq. 1.25, Eq. 1.29, and Eq. 1.32, we finally obtain:

$$\frac{\partial G_{\mathrm{KS}}^{\mathrm{L}}}{\partial \bar{\bar{\rho}}_j} = \left(\frac{\sigma_{\mathrm{VM},j}}{\sigma_L} - 1\right)\frac{e^{P\bar{g}_j}}{\sum_k e^{P\bar{g}_k}} - \boldsymbol{K}^{-1}\frac{\partial G}{\partial \boldsymbol{u}}\left(\frac{\partial \boldsymbol{K}}{\partial \bar{\bar{\rho}}_j}\right)\boldsymbol{u}. \tag{1.33}$$

3: More information about the adjoint method used to analytically calculate the first-order derivatives can be found on the Martins *et al.* book [13].

To avoid the explicit calculation of $\boldsymbol{K}^{-1}$ we use the *adjoint method*[3]. Here is the linear system that, once solved, permits to calculate $\boldsymbol{\psi}$:

$$\boldsymbol{K}\boldsymbol{\psi} = \frac{\partial G}{\partial \boldsymbol{u}} \iff \boldsymbol{\psi} = \boldsymbol{K}^{-1}\frac{\partial G}{\partial \boldsymbol{u}}. \tag{1.34}$$

This formula is called *adjoint equation*. This equation is solved for $\boldsymbol{\psi}$ and the result used to evaluate:

$$\frac{\partial G_{\mathrm{KS}}^{\mathrm{L}}}{\partial \bar{\bar{\rho}}_j} = \left(\frac{\sigma_{\mathrm{VM},j}}{\sigma_L} - 1\right)\frac{e^{P\bar{g}_j}}{\sum_k e^{P\bar{g}_k}} - \boldsymbol{\psi}\left(\frac{\partial \boldsymbol{K}}{\partial \bar{\bar{\rho}}_j}\right)\boldsymbol{u}. \tag{1.35}$$

Solving linear system 1.34 instead of directly calculating the inverse matrix of $\boldsymbol{K}$ is more efficient from a performance perspective. The cost of solving a system using the Cholesky decomposition is $\mathcal{O}(N^3/3)$, while a matrix inversion is $\mathcal{O}(N^3)$.

where N represents the size of the square matrix describing the linear system. Equation 1.35 represents the first-order derivative equation used to evaluate the sensitivity of the constraint function $G_{\mathrm{KS}}^{\mathrm{L}}$ with respect to the physical densities $\bar{\bar{\boldsymbol{\rho}}}$. The value of $\boldsymbol{\psi}$ is calculated every iteration solving the linear system 1.34.

The sensitivity of the aggregated constraint function with respect to the design variable $\boldsymbol{\rho}$ is evaluated using Equations 1.20, 1.5, 1.6, and 1.7 as follows:

$$\frac{dG^{\mathrm{L}}_{\mathrm{KS}}}{d\rho_i} = \sum_{j\in\mathbb{N}_{i,R}} \frac{\partial G^{\mathrm{L}}_{\mathrm{KS}}}{\partial \overline{\widetilde{\rho}}_j} \frac{\partial \overline{\widetilde{\rho}}_j}{\partial \widetilde{\rho}_j} \frac{\partial \widetilde{\rho}_j}{\partial \rho_i}. \tag{1.36}$$

1.1.2 Truss discretization SAND minimum volume formulation

We are now shifting our focus from continuous structures to discrete truss systems, describing the Truss Topology Optimization (TTO) (also known in early literature as layout optimization), a structure optimization method that focuses on discrete structures. In his most used formulation, TTO aims at reducing material usage while meeting stress criteria using a SAND approach. The problem is already well-posed for comparison with continuous discretization, and we intend to explore specific key concepts within its established framework.

Classical Michell structures The characteristics of these structures are described by some simple criteria that date to the end of the 19th and the beginning of the 20th century. When a structure is statically determinate — i.e. the structure is not a mechanism, and it is not over-constrained by the supports — the Maxwell theorem [36] states that:

36. Maxwell (1870), 'I.—On Reciprocal Figures, Frames, and Diagrams of Forces'

$$\sum_{\forall i|q_i>0} \ell_i q_i + \sum_{\forall i|q_i<0} \ell_i q_i = \text{const.} \tag{1.37}$$

where ℓ_i and q_i represent the length and the axial force of the i-th member, respectively. The constant value at the right of Equation 1.37 depends on the nature of the boundary conditions and the material used. The Maxwell theorem dictates that any increment in compression forces must be counterbalanced by an equivalent increase in tension forces when the structure remains topologically unchanged. So for statically determinate structures the structure layout is not influenced by the ratio between σ_{c} and σ_{t}, Young's modulus E of the material, nor the force magnitude.

Starting from Maxwell's findings, Michell theorized two further criteria for optimal truss structures [37] valid when the maximum allowable stress is equal in tension and compression ($\sigma_{\mathrm{t}} = \sigma_{\mathrm{c}}$) and when the supports of the structure are statically determinate. The first one states that all the members of an optimal structure should present internal stress equal in magnitude to the maximum allowable value of the material – i.e. the structure is *fully stressed*. The second criterion asserts that the strain of all the members of the structure should be equal and there should be no other point having a strain higher than this value. As formulated, these two criteria are known as the Michell criteria. The second criterion was later generalized by Hemp [4] as:

37. Michell (1904), 'The limits of economy of material in frame-structures'

4. Hemp (1973), 'Optimum Structures'

$$-\frac{1}{\sigma_c} \leq \varepsilon \leq \frac{1}{\sigma_t}. \tag{1.38}$$

Compared to the second Michell criterion, Equation 1.38 permits to correct identification of the minimum volume structure even when different strength values for compression and tension and different support types are taken. These criteria are known as the Michell-Hemp criteria.

Plastic material formulation The rigid-plastic formulation characterizes the material as entirely rigid up to the point of reaching the yield stress, denoted as σ_y, and subsequently assumes a constant stress level of σ_y once that threshold is exceeded. This formulation is a clear consequence of the application of the Michell-Hemp criteria and has thus been used in the very first work of layout optimization (also known as TTO) [2–4].

2. Dorn et al. (1964), 'Automatic design of optimal structures'
3. Chan (1964), 'Optimum structural design and linear programming'
4. Hemp (1973), 'Optimum Structures'

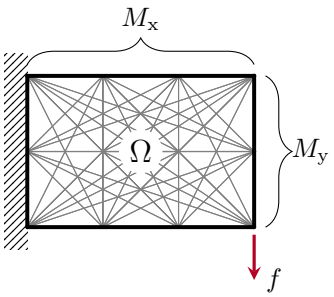

Figure 1.4: The domain Ω is discretized using a set of straight members connecting a set of nodes. This framework is known as the ground structure.

The ground structure approach The ground structure is a framework composed of various structural members that connect specified points or nodes in two- or three-dimensional space (see Fig. 1.4). These members can take the form of beams, columns, wires, or bars elements, depending on the specific structural requirements. In this thesis, we will deal with trusses, and so the chosen element is the bar. Since the nodes within the ground structure are considered pin-joints, all straight members exclusively face either tension or compression loads.

Depending on how the connectivity of the grid of nodes is, we can experience very different ground structures. In a fully connected ground structure, every node within the system is linked to every other node, resulting in a dense and redundant structural configuration. The number of bars N_{el} of a fully connected ground structure can be determined using the following formula:

$$N_{el} = \frac{M \cdot (M-1)}{2}, \tag{1.39}$$

where M represents the number of nodes of the structure.

In classic works, the ground structure is used as the start of the optimization, where the optimized structure is obtained as a subset of the initial ground structure, but multiple alternative approaches have been proposed since then, e.g. starting from a very coarse ground structure that is enriched during the analysis [38], or giving the nodes of a coarse ground structure the possibility to move, during [39–41], or after the optimization, simultaneously reducing the number of active members of the solution [42, 43].

38. Gilbert et al. (2003), 'Layout optimization of large-scale pin-jointed frames'
39. Pedersen (1973), 'Optimal Joint Positions for Space Trusses'
40. Achtziger (2007), 'On simultaneous optimization of truss geometry and topology'
41. Descamps et al. (2013), 'A lower-bound formulation for the geometry and topology optimization of truss structures under multiple loading'
42. He et al. (2015), 'Rationalization of trusses generated via layout optimization'
43. Lu et al. (2023), 'Reducing the number of different members in truss layout optimization'

Optimization formulation add g_stress g_eq

The volume minimization formulation with maximum stress constraints is stated in terms of members' cross-sectional areas $\boldsymbol{a}$ and member forces $\boldsymbol{q}$ as follows:

$$\begin{aligned} \min_{\boldsymbol{a},\boldsymbol{q}} \quad & V = \boldsymbol{\ell}^T \boldsymbol{a} && \text{(Volume)} \\ \text{s.t.} \quad & \boldsymbol{B}_s \boldsymbol{q} = \boldsymbol{f} && \text{(Force equilibrium)} \\ & -\sigma_c \boldsymbol{a} \le \boldsymbol{q} \le \sigma_t \boldsymbol{a} && \text{(Stress constraints)} \\ & \boldsymbol{a} \ge 0, \end{aligned} \qquad (\mathbb{P}_0)$$

where $\boldsymbol{B}_s$ is a $N_{\text{dof}} \times N_{\text{el}}$ matrix containing the direction cosines of the j-th member with respect to the i-th degree of freedom to calculate the nodal force equilibrium, and where N_{dof} is the number of Degrees Of Freedom (DOFs), equal to $2M$ or $3M$ for a two- or a three-dimensional load case, respectively. $\boldsymbol{q} = [q_1, q_2, \dots, q_{N_{\text{el}}}]^T$ is the vector containing the internal member forces, with a positive sign when in tension, caused by the external load $\boldsymbol{f} = [f_1, f_2, \dots, f_{N_{\text{dof}}}]^T$. The state variable $\boldsymbol{a} = [a_1, a_2, \dots, a_{N_{\text{el}}}]^T$ represents the cross-sectional area of the N_{el} members of the structure. σ_c and σ_t are the compressive and tensile maximum allowable stresses of the material, respectively. This formulation takes into account only the linear behavior of the structure and is equivalent to the original and well-studied member force formulation [2, 14].

The resolution of Problem $\mathbb{P}_0$ frequently produces complex structures made up of a multitude of small members that tend to the shapes of Michell structures (see Fig 1.5) [37, 38]. While it is known that these structures are nearly optimal, one would want to limit the complexity of the resulting structure. Substituting $\boldsymbol{\ell}$ with $\tilde{\boldsymbol{\ell}} = [\ell_1 + s, \ell_2 + s, \dots, \ell_{N\text{el}} + s]^T$ in the objective function of $\mathbb{P}_0$, one would penalize the appearance of small members [44]. $\tilde{\boldsymbol{\ell}}$ is called augmented member length and s the joint cost. This approach mimics the mesh-independency regularization filter of topology optimization, avoiding the inevitable apparition of structures with tiny features when a fine mesh is adopted.

1.2 Comparison between continuous and truss discretization

In the upcoming discussion, we will be comparing the optimized structures using discrete and continuous meshes. Our primary objective in this comparison is to gain a comprehensive understanding of the application limits inherent in these two structural discretization methods. If, indeed, we identify such limitations, the aim is to discern and define them. Such discussions have already been pointed out in the literature [7, 45], but they are usually only empirical considerations

2. Dorn et al. (1964), 'Automatic design of optimal structures'
14. Bendsøe et al. (2004), 'Topology Optimization'
37. Michell (1904), 'The limits of economy of material in frame-structures'
38. Gilbert et al. (2003), 'Layout optimization of large-scale pin-jointed frames'
44. Parkes (1975), 'Joints in optimum frameworks'

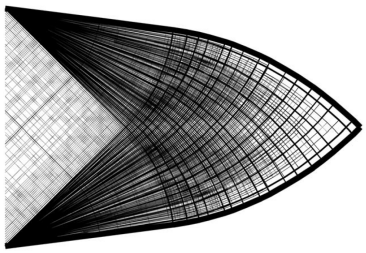

Figure 1.5: The optimal structures found by layout optimization tend at Michell-like structures, made up of a very large number of infinitesimal struts [38].

7. Bendsøe (1989), 'Optimal shape design as a material distribution problem'
45. Watts et al. (2019), 'Simple, accurate surrogate models of the elastic response of three-dimensional open truss micro-architectures with applications to multiscale topology design'

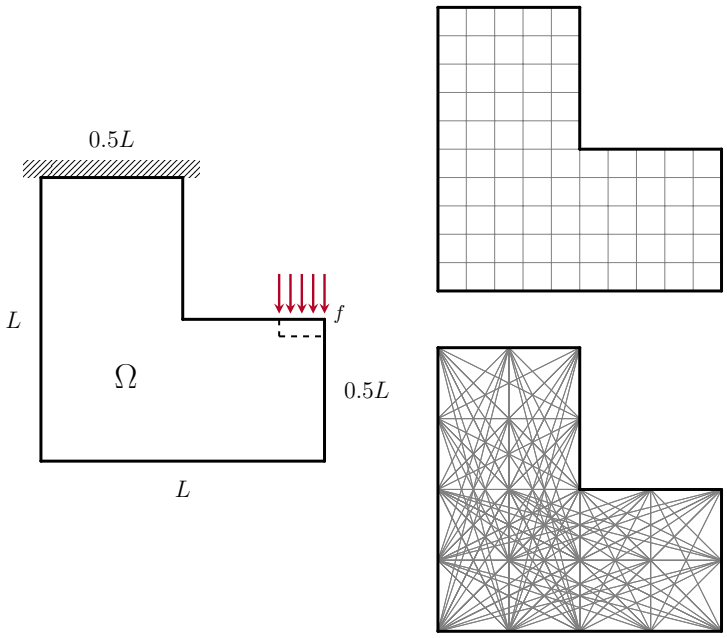

Figure 1.6: On the left, plot of the L-shape beam test case, on the right the graphical representations of the two discretizations used, the continuous (above) and the truss-like (below).

and not numerical analysis.

Since our interest is in ultralight structures, we are especially interested in comparing the results of both optimization methods when dealing with different volume fractions on a common load case. Since we can't directly control volume in our formulation, we will adjust the material properties to influence the volume fraction of the optimized structure. For this comparative analysis, we have selected three key performance metrics: the volume fraction $V_f = V/\Omega$, the structural compliance C, and the maximum material allowable σ_L. Among these, we classify stress limit as the active metric used to influence the optimization, while volume and compliance are the objective of the optimization and a passive metric, respectively. In addition to the aforementioned performance metrics, we will also track the execution time of the algorithms.

1.2.1 Definition of a common test case

The L-shape beam is one of the most used load case benchmarks for stress-based topology optimization [25, 26]. This choice is driven by the distinctive geometry of the problem, which generates a stress concentration, particularly at the sharp corner—a phenomenon approaching infinity. Consequently, optimized solutions often feature a large fillet, mitigating the intensity of the stress singularity. The geometric description of the test case is given in Fig. 1.6. The beam with dimensions $L \times L$ presents an encastre on the top part and a load on the right extremity. For the continuous mesh case the load is distributed over multiple elements (5% of L) to avoid stress concentrations and the stress constraints are not evaluated there. This zone is considered outside of the design domain Ω.

25. Duysinx et al. (1998), 'Topology optimization of continuum structures with local stress constraints'
26. Le et al. (2010), 'Stress-based topology optimization for continua'

To permit the discretization comparison, the structure is divided into two distinct meshes: in the continuous case, we employ a mesh consisting of 600×600 quadrilateral elements, totaling 270 000 elements, while for the truss configuration, we employ a mesh with 33×33 nodes and a fully connected ground structure, comprising a total of 305 728 candidates.

We employ the same isotropic material and structure dimensions for the two optimizations, and the complete data is resumed in Table 1.1. The value of the maximum material admissible σ_L is used as the parameter that influences the volume fraction of the solutions. For simplicity, all numeric values are assumed normalized and dimensionless.

Parameter	Value
E	1
ν	0.3
L	100
σ_L	var.

Table 1.1: Material data used for the optimizations. The value of the maximum material admissible σ_L is used as the parameter to generate multiple optimized topologies.

1.2.2 Numerical application

The focus of this section is to provide the numerical framework used to carry out the comparative analysis of the optimization results obtained from continuous and truss discretizations. The optimization formulations previously described have been implemented using Python.

The optimizing algorithm chosen for the continuous mesh is the Method of Moving Asymptotes (MMA) [46]. The parameter called *movelimit*[4] is set to 0.1 while the other algorithm's parameters are set to their default value. A continuation scheme for the aggressiveness of the projection parameter β is set to increase by one every 200 iterations, the number of max iteration is set to 7500, the stopping criteria is calculated as $\|r_k\|_2/\sqrt{N_e}$ on the physical densities $\widetilde{\overline{\rho}}$ [22], and it is set to 10^{-4}. The aggregation parameter P of the aggregation function G^L_{KS} is set to 32. The numerical implementation is carried out using the NLopt Python optimization framework [47], analytically evaluating the sensitivity using Equations 1.20, and 1.24.

Formulation $\mathbb{P}_0$ represents a LP problem that can be efficiently solved by modern algorithms. In this work, we used the Python package CVXPY 1.2.2 [48] with the ECOS 2.0.7 [49] solver. The joint cost s is set to 0.001 and the stopping criteria is chosen as $\|\Delta \boldsymbol{x}\|_\infty \leq 10^{-8}$. As Formulation is linear, no sensitivity calculation is carried out.

The optimizations presented in this section are performed on a server equipped with an Intel® Xeon® CPU E5-2650 @ 2.20 GHz and using 8 GB of RAM.

Coninuous mesh optimization results In this section, we generate multiple optimized structures with different volume fractions V_f by launching the optimization code for continuous mesh with different values of the material admissible σ_L spanning from 0.2 to 20.

46. Svanberg (1987), 'The method of moving asymptotes—a new method for structural optimization'

4: More information on the implementation of the *movelimit* parameter can be found on the paper by Verbart [27]

47. Johnson (2007), 'The NLopt nonlinear-optimization package'

48. Diamond et al. (2016), 'CVXPY: A Python-Embedded Modeling Language for Convex Optimization'

49. Domahidi et al. (2013), 'ECOS: An SOCP solver for embedded systems'

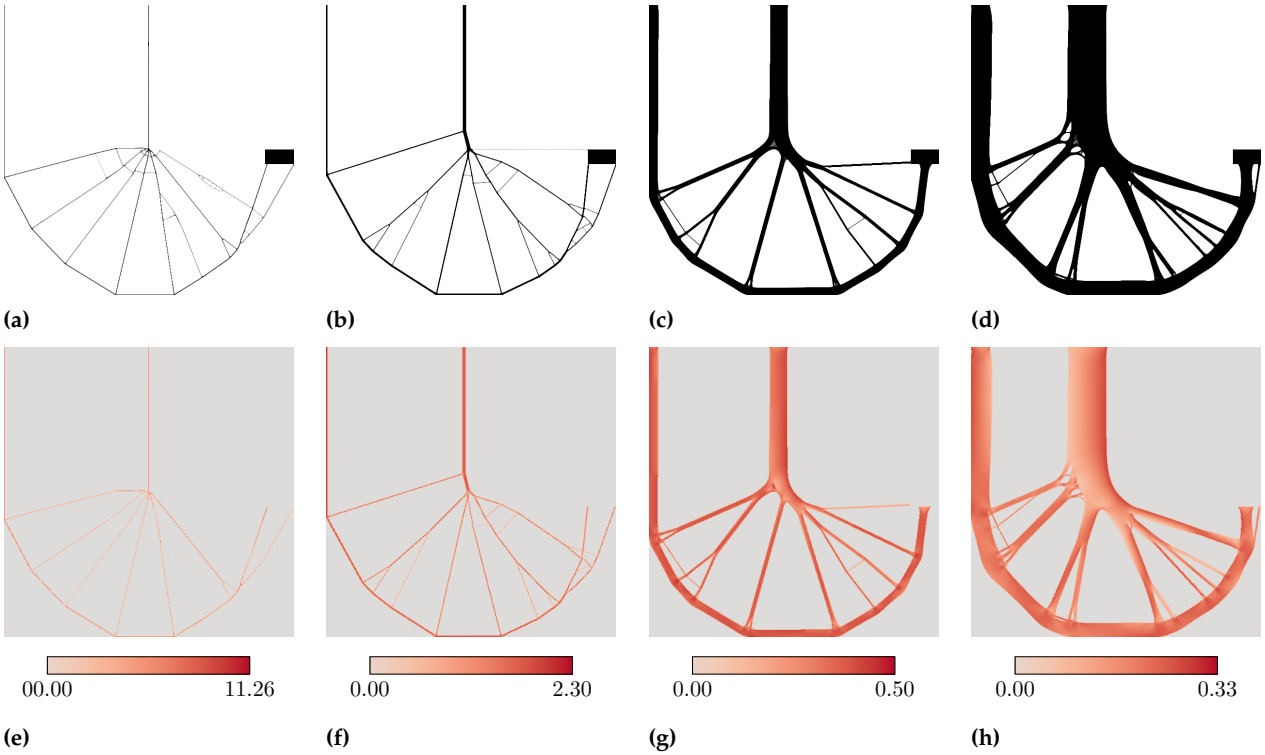

Figure 1.7: (a-d) topology optimized structures for different material admissibles $\sigma_L = 10.00, 2.00, 0.40$ and 0.25, showing a volume fraction of $V_f = 1.60\%, 4.04\%, 18.03\%$ and 34.71%, respectively. (e-h) Von Mises stress distribution of the optimized structures.

On top of volume fraction, compliance, and stress, we evaluate an additional metric specific to continuous meshes called the *measure of non-discreteness* [21] to evaluate the quality of the solutions. It is defined as:

$$M_{\text{nd}} = \frac{\sum_e 4\overline{\overline{\rho}}_e(1-\overline{\overline{\rho}}_e)}{n} \times 100\%, \tag{1.40}$$

where results near zero mean a completely black-and-white design.

21. Sigmund (2007), 'Morphology-based black and white filters for topology optimization'

The results obtained for $\sigma_L = 10.00, 2.00, 0.40$ and 0.25 are shown in Fig. 1.7. In the upper part of the figure (a-d), we see the topology of the optimized structures with an ascending volume fraction V_f. Interestingly, the topology of the solution remains almost unchanged, varying principally in the thickness of its members. We notice the classic large fillet around the corner that alleviates the stress concentration problem. As the volume decreases, the optimized structure tends to a solution that resembles Michell structures, with a reducing fillet radius. In those cases, we know that the topology optimization algorithm acts as a method for the layout of truss-like structures [6]. This effect is caused by the combination of different factors, such as the regularization filter, the mesh size, and the low volume fraction [50]. A summary of the numerical results is presented in Table **??**.

6. Bendsøe et al. (1988), 'Generating optimal topologies in structural design using a homogenization method'

50. Sigmund et al. (2016), 'On the (non-)optimality of Michell structures'

In the lower part of Fig. 1.7 (e-f), we plot the equivalent Von Mises

σ_L	**max** σ_L	V_f	C	M_{nd}	**It.**	**Time**
20.00	23.51	1.18 %	6992	1.91 %	1142	8 h 11 m
10.00	11.26	1.60 %	3837	2.19 %	1147	7 h 55 m
8.00	8.78	1.74 %	2766	1.95 %	792	5 h 39 m
6.00	7.15	1.89 %	2243	1.81 %	806	5 h 35 m
5.00	5.81	2.17 %	1823	1.81 %	849	5 h 53 m
4.00	4.69	2.67 %	1424	2.02 %	894	6 h 12 m
3.00	3.47	3.00 %	1133	1.64 %	993	6 h 45 m
2.00	2.30	4.04 %	781	1.45 %	1189	8 h 20 m
1.00	1.18	7.28 %	404	1.35 %	1621	11 h 41 m
0.90	1.06	8.09 %	365	1.31 %	1656	11 h 36 m
0.80	0.96	8.82 %	332	1.21 %	1937	15 h 21 m
0.70	0.84	10.05 %	292	1.09 %	1827	13 h 21 m
0.60	0.73	11.80 %	250	1.19 %	1955	14 h 21 m
0.50	0.61	14.18 %	213	1.06 %	2032	15 h 39 m
0.40	0.50	18.03 %	170	1.08 %	2259	17 h 6 m
0.35	0.44	21.12 %	148	1.15 %	2421	19 h 29 m
0.30	0.38	26.21 %	126	1.50 %	3100	24 h 46 m
0.25	0.33	34.71 %	104	1.04 %	3484	27 h 39 m
0.20	0.27	48.08 %	77	1.26 %	7500	91 h 46 m

Table 1.2: Numerical results of the topology optimization method of the L-shape beam load case with varying material admissible σ_L on a 600×600 elements mesh.

stress for every element of the solution with physical density $\widetilde{\overline{\rho}} > 0.5$. Multiple interesting observations can be made. First, we notice that the stress distribution is almost uniform in the structure, and it tends to the value of the material admissible σ_L – i.e. we approach a *fully stressed* structure. Even if the geometric support of the theory is different, it looks like the topology-optimized structures follow the Michell criteria presented in Section 1.1.2 for optimal truss structures. Furthermore, it is observed that the maximum stress exceeds the material admissible σ_L. Aggregation methods aim to estimate the maximum value of the stress constraint across a group of elements. However, these aggregation methods do not perfectly align with the exact maximum value, which is a recognized limitation. To address this challenge, multiple approaches have been proposed within the aggregation framework to accurately account for the true constraint value, like using a set of active stress constraints [51], several aggregation clusters [52] or rectifier functions [53].

Looking again at Table **??**, we notice that the optimization processes exhibit long execution times, especially when dealing with extreme cases like high-volume fractions. This effect is likely caused by the very fine mesh used to discretize the design domain Ω, by the sensitivity calculation by means of the adjoint method, and by the increasing difficulty of satisfying the stress constraints.

As previously mentioned, our focus lies in exploring the method's limits, particularly at the volume fraction boundaries. When dealing with excessively weak materials – i.e. materials that show a low σ_L,

51. Bruggi et al. (2012), 'Topology optimization for minimum weight with compliance and stress constraints'

52. París et al. (2010), 'Block aggregation of stress constraints in topology optimization of structures'

53. Norato et al. (2022), 'A maximum-rectifier-function approach to stress-constrained topology optimization'

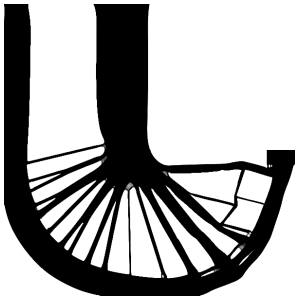

Figure 1.8: The optimized structure for $\sigma_L = 0.2$ with $V_f = 48.08\,\%$, but does not converge after 7500 iterations.

we encounter a scenario where no solution can be attained since no distribution can fulfill the imposed constraints. Throughout our research with this specific test case and mesh size, we did not produce any solutions with a volume fraction exceeding 50%. Although we haven't reached that scenario with σ_L set to 0.2, the calculation time and the number of iterations increase significantly,showing that we have encountered the method's limits. The calculation time has significantly increased because the algorithm faces greater difficulty in satisfying the stress constraints. Fig. 1.8 shows the topology of the solution with $\sigma_L = 0.2$, $V_f = 48.08\,\%$ and over five days of optimization.

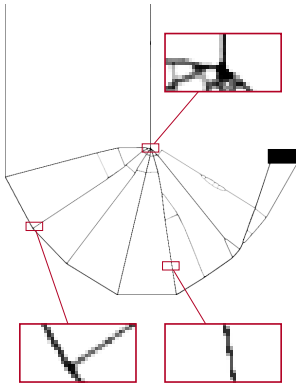

Figure 1.9: The optimized structure for $\sigma_L = 10.0$ with $V_f = 1.60\,\%$. Some of the structure's features present not even a fully-dense element in their thickness.

Conversely, when dealing with exceedingly strong material – i.e. materials that show a high σ_L, the optimal scenario would demand such minimal material usage that certain sections of the structure become thinner than the width of a single element. In this case, the mesh used for discretization is too coarse to accurately represent the solution, and finer meshing becomes essential to capture the intricate details of the optimized design. Fig. 1.9 shows the limit case when $\sigma_L = 10.0$ and $V_f = 1.60\,\%$.

Finally, in Fig. 1.10 are the plots summarizing our findings, with the limits highlighted. To effectively show the different orders of magnitude present in the plot, we have used both linear and logarithmic scales simultaneously. It's interesting to note that the volume fraction V_f follows a hyperbolic relationship, while compliance C exhibits a linear correlation with respect to the material admissible σ_L.

Truss mesh optimization results In this section, we present the optimized structures of the truss discretization. Fig. 1.11 provides a visual representation of the topology and the corresponding stress distribution. Due to the inherent linearity properties of Formulation $\mathbb{P}_0$, several intriguing characteristics emerge. Notably, in the case of the tested L-shaped case, we encounter a scenario where the boundary conditions are neither overconstrained nor subject to asymmetric

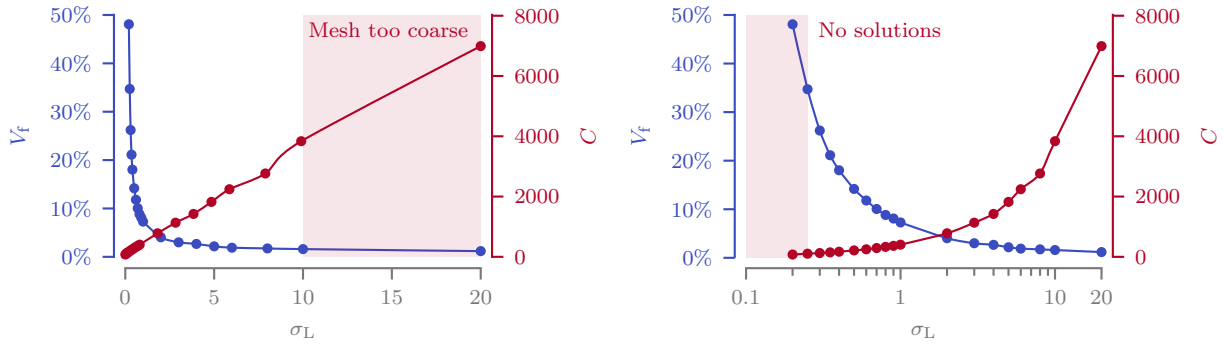

Figure 1.10: Linear (a) and logarithmic (b) plot of the volume fraction V_f and the compliance C with respect to the maximum material admissible σ_L for the continuous mesh structures. Areas in red represent the boundaries of the applied method.

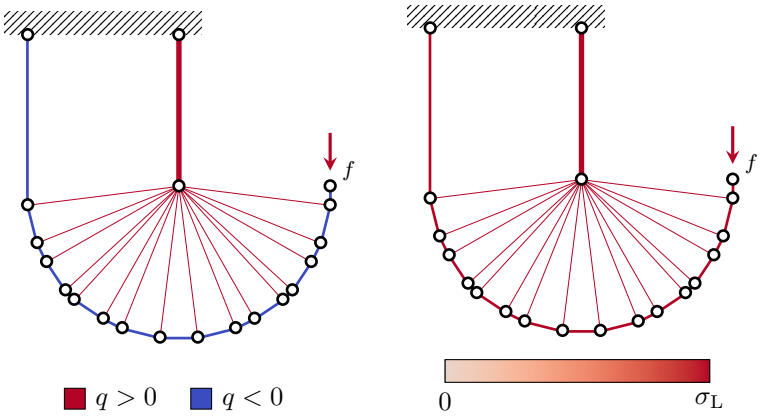

Figure 1.11: Topology (a) and stress (b) plot for the truss-like discretization.

Table 1.3: Numerical results of the TTO method of the L-shape beam load case with varying material admissible σ_L on a 33×33 ground structure.

σ_L	V_f	C	Min λ	Time
50.0	0.12 %	23 282	111.7	1 m 6 s
20.0	0.31 %	9313	70.6	1 m 9 s
10.0	0.62 %	4656	49.9	1 m 18 s
8.0	0.78 %	3725	44.7	1 m 15 s
6.0	1.03 %	2794	38.7	1 m 10 s
5.0	1.24 %	2328	35.3	1 m 24 s
4.0	1.55 %	1863	31.6	1 m 18 s
3.0	2.07 %	1397	27.4	1 m 15 s
2.0	3.10 %	931	22.3	1 m 15 s
1.0	6.21 %	466	15.8	1 m 17 s
0.9	6.90 %	419	15.0	1 m 20 s
0.8	7.76 %	373	14.1	1 m 21 s
0.7	8.87 %	326	13.2	1 m 16 s
0.6	10.35	279 %	12.2	1 m 20 s
0.5	12.42	233 %	11.2	1 m 22 s

stress constraints. Consequently, this test case aligns with the Michell criteria. As a result, the topology does not vary regardless of the imposed stress limit, and the structure is fully stressed. Additionally, the following equation consistently holds:

$$V^* = \frac{fL}{\sigma_L} \cdot \text{const.}, \tag{1.41}$$

where the multiplicative constant depends on the load case and the ground structure used to discretize the design space Ω [54]. The execution time of the optimization is approximately 90 s and does not change with respect to the maximum stress σ_L. The results of the multiple optimizations can be found in Table 1.3.

It's worth noting that we have intentionally opted for a fine mesh here to achieve a design variable count roughly equivalent to that of the continuous mesh case. We have utilized a fully connected ground structure with 33×33 nodes, but in reality, we obtain satisfactory

54. Lewiński et al. (1994), 'Extended exact solutions for least-weight truss layouts—Part I'

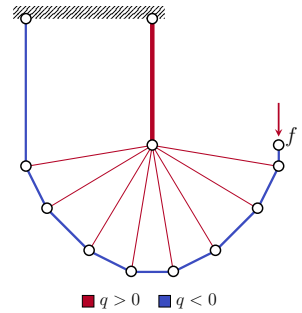

Figure 1.12: Optimized structure obtained a fully connected ground structure with 13 × 13 and 7705 candidates.

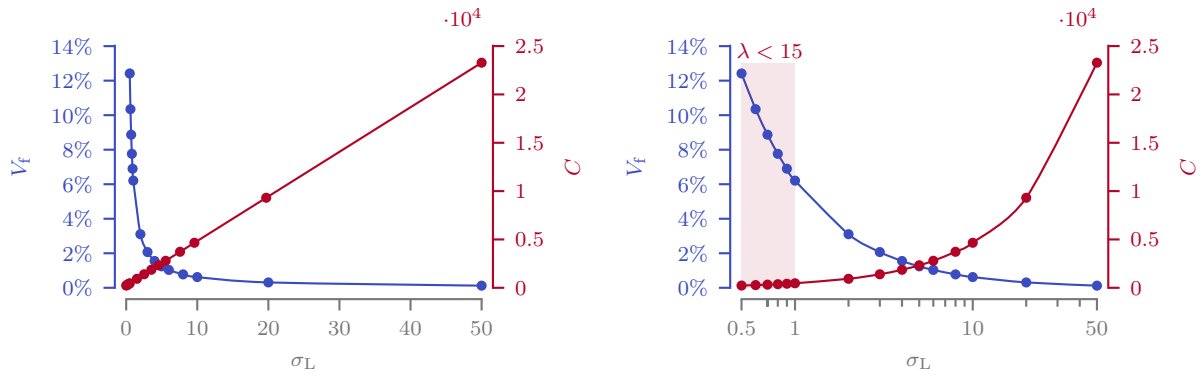

Figure 1.13: Linear (a) and logarithmic (b) plot of the volume fraction V_f and the compliance C with respect to the maximum material admissible σ_L for the truss-like structures. Areas in red represent the boundaries of the applied method.

results even with just 13×13 nodes (see Fig. 1.12). In this case we obtain a normalized volume $V^* = 4.705\ fL/\sigma_L$, signifying a 1.05 % increase compared to the 33×33 case with $V^* = 4.656\ fL/\sigma_L$ with a variable count reduction of 97.4 % (305 728 vs 7705 candidates). The computational time remains below one second.

In assessing solution quality, we employ a distinct metric known as the slenderness ratio, denoted as λ, which represents the ratio between the length and the radius of gyration of the bar. In our specific case, we have established a minimum slenderness ratio of 15. For a bar with a circular cross-sectional area, this corresponds to a radius of R_λ for a bar length of 7.5 R_λ. We higlighted in red the optimized structures that does not repect the minimum slenderness ratio in Table 1.3. It is important to note that this metric is very sensible to the ground structure used: for example in the 13×13 nodes test case, λ becomes critical ($\lambda = 14.8$) only when $\sigma_L = 0.25$ and $V_f = 25.09$, suggesting that a control of this parameter during the optimization should be beneficial.

Lastly, Fig. 1.13 provides a visual summary of our findings, emphasizing in red the observed limits. To effectively show the different orders of magnitude present in the plot and how already done for the continuous mesh case, we have used both linear and logarithmic scales simultaneously. In this case, the compliance exhibits a perfectly linear relationship, while the volume follows a hyperbolic law in accordance with Equation 1.41.

1.2.3 Discussion

In this section, we present a series of graphs for the two formulations comparing the three figures of merit that have been considered thus far: the maximum material admissible σ_L, the compliance C, and the volume fraction V_f. It's important to note that the data presented in these graphs excludes the values that fall outside the limits highlighted for the two different discretizations in the previous subsections.

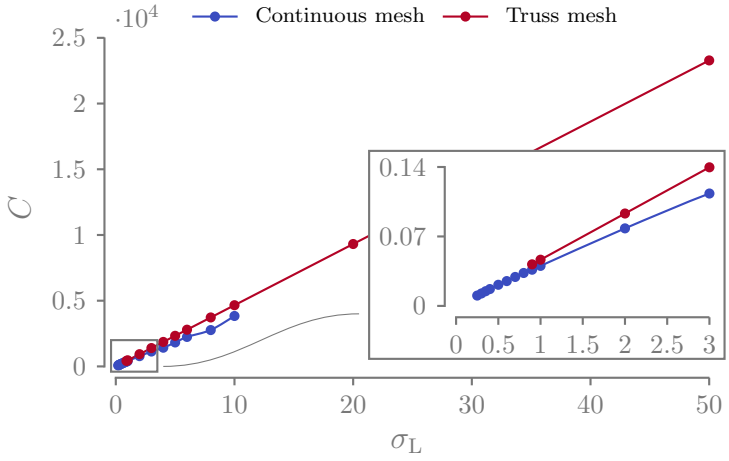

Figure 1.14: Compliance – Maximum material admissible plot for the continuous and truss discretizations.

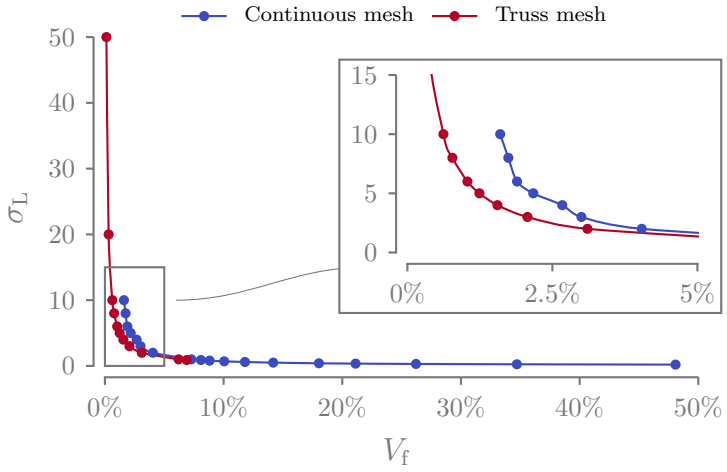

Figure 1.15: Maximum material admissible – Volume fraction plot for the continuous and truss discretizations.

Fig. 1.14 depicts the stress compliance graph for the L-shaped beam load case under consideration. It is evident that the truss configuration consistently exhibits lower compliance values for every considered material admissible and maintains a perfectly linear relationship, in contrast to the continuous discretization approach. We speculate that the difference may be attributed to the non-linearity of the formulation, potentially causing the continuous approach to converge to a local minimum.

In Fig. 1.15 we plot the different volume fractions obtained for a given material admissible (the axis in the graph are swapped as for us the most important figure of merit is the volume fraction). The continuous mesh yields structures that are more massive for a given material limit. This outcome can be attributed not only to the aforementioned non-linearity in the formulation but also to another intriguing phenomenon. When dealing with volumes exceeding 1 % (see Fig. 1.7b), we observe that the material in the topology-optimized structure is distributed across multiple elements, appearing somewhat "smeared". In contrast, the truss representation concentrates all the structural mass along an imaginary line extending from one node to another, being more efficient.

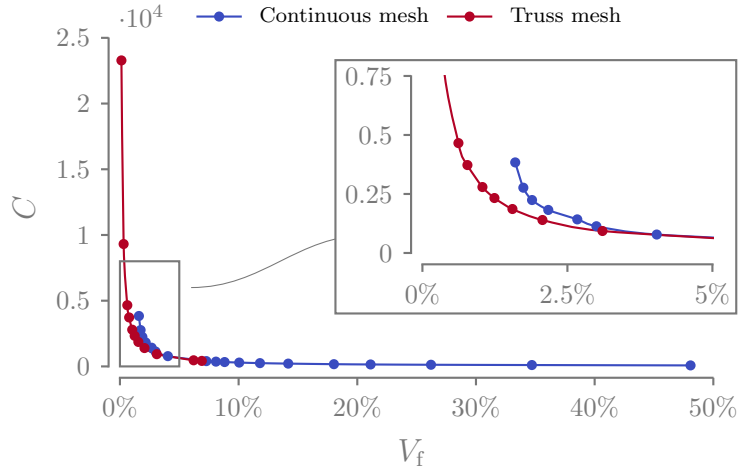

Figure 1.16: Compliance – Volume fraction plot for the continuous and truss discretizations.

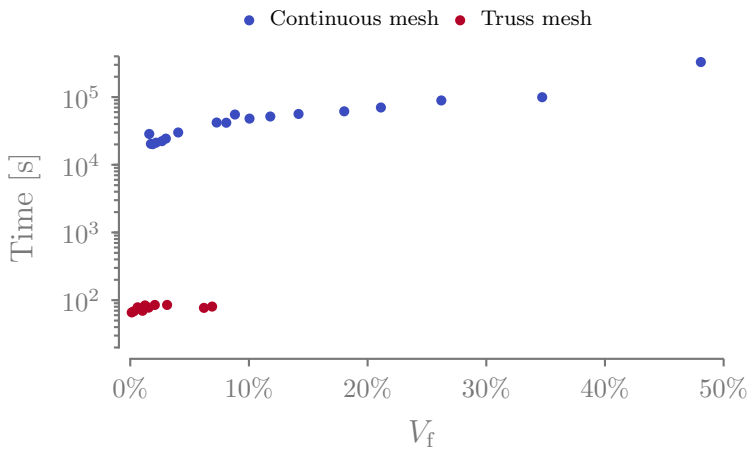

Figure 1.17: Time – Volume fraction plot for the continuous and truss discretizations.

We can also distinctly observe that the truss representation serves as the lower limit of the topology optimization for low volume fractions. Interestingly, both discretizations follow a similar trend for high-volume fractions, despite the significant disparity in their physical description models. The very same trends can be observed watching the volume-complaince graph of Fig. 1.16.

Finally, in Fig. 1.17 we turn our attention to the time comparison between the two optimization methods. It is noteworthy that a consistent three-order of magnitude difference is observed between the two methods (days vs. minutes). Additionally, it's worth recalling that in the truss case, employing an extremely fine ground structure is not a necessity, which implies that the time difference could potentially be even bigger.

The notable difference in computation time for stress-based topology optimization (which is not self-adjoint in contrast to compliance minimization) points to the potential for exploring SAND topology optimization. While preliminary studies in this direction have been conducted [55], they lie beyond the scope of this thesis and will not be further investigated. It's worth mentioning that SAND approaches typically lead to a substantial increase in the number of design

55. Munro et al. (2017), 'Local stress-constrained and slope-constrained SAND topology optimisation'

variables. However, in truss topology problems, this is less of a concern due to the ground structure approach, which results in numerous cross-sectional area design variables and fewer displacement-related ones. This, however, does not hold when dealing with a continuous mesh.

To sum up, in comparing truss and continuous discretization methods, the advantages of truss structures become evident when considering the limitations of continuous discretization for the optimization of ultralight structures. One key drawback of continuous discretization is its increasing need for more elements as the desired level of refinement becomes finer at low volume fractions. Additionally, continuous discretization faces challenges with stress limits in optimized structures, which often exceed the specified admissible limits. Strategies exist to address this issue, but they come at the cost of increased computation time. Furthermore, stress constraints in continuous discretization are often defined for equivalent Von Mises stress, making it more challenging to distinguish between asymmetric bounds for tension and compression. Finally, truss structures are naturally subject to local buckling as a mode of failure [50], a phenomenon that can be more easily and directly modeled in a truss discretization.

50. Sigmund et al. (2016), 'On the (non-)optimality of Michell structures'

While truss discretization offers advantages in terms of computational efficiency, it does come with certain limitations. In the minimum volume formulation, the problem is linear and cost-effective to solve. However, the linearity is lost when additional constraints, such as local buckling, are introduced. Moreover, the formulation does not inherently account for the kinematic compatibility of the problem. This limitation restricts its applicability to relatively simple problems and can pose issues when dealing with complex scenarios involving multiple loads or constraints that may lead to overconstraint structures.

Despite these challenges, we decided to favor truss discretization for our research. In the upcoming chapter, we will address and explore potential solutions to address its main limitations to further enhance its applicability and effectiveness.

1.3 Conclusion

Since the first developments of the topology optimization method, it has been recognized that "For moderately low volume fractions the lay-out of truss-like structures is predicted, but for very low volume fractions it is recommended that the traditional lay-out theory be employed..." [7]. However, the performance gap has never been quantified, nor has the domain of applicability been assessed. This is the primary motivation behind this chapter. Additionally, it's important to note that these assumptions were primarily based on compliance

7. Bendsøe (1989), 'Optimal shape design as a material distribution problem'

formulations and not on volume minimization formulations, which are more pertinent to the aeronautical context.

In this chapter, we introduced a volume minimization formulation applicable to both continuous and truss-like discretizations, aiming at a meaningful comparison. We established a standardized two-dimensional test case, the L-shaped beam, commonly used in stress-based optimization. We conducted multiple optimization runs for both discretization methods using various materials and subsequently compared the results, focusing primarily on volume fraction, compliance, and stress in the optimized structures.

Considering the limitations encountered with the continuous approach, particularly at very low volume fractions, we opted for the truss discretization method for our specific research problem. We also identified certain limitations inherent to truss discretizations, which will be addressed in the following chapter.

Enriching the classic TTO formulation with advanced mechanical constraints

2

Introduction check the word paper every eq and fig must begin with the chapter scaling images

Table 2.1: Non-exhaustive list of the existing research in Truss Topology Optimization (TTO) with their corresponding scientific contributions

Authors	Stress	Local Buckling	Topological buckling	Kinematic compatibility	Multi-load cases
Dorn et al. (1964)	x	-	-	-	-
Hemp (1973)	x	-	-	-	x
Reinschmidt et al. (1974)	x	x	-	∼	-
Kirsch (1980)	x	-	-	x	-
Oberndorfer et al. (1996)	x	x	-	-	-
Silva Smith (1997)	x	x	∼	-	x
Achtziger (1999a, 1999b)	x	x	x	-	x
Stolpe (2004)	x	x	-	x	x
Pritchard et al. (2005)	x	-	-	-	x
Tyas et al. (2006)	x	x	x	-	x
Descamps et al. (2014)	x	x	x	-	x
Schwarz et al. (2018)	x	x	-	-	-
Cai et al. (2022)	x	x	x	-	-
Present work	x	x	x	x	x

2.1 Advanced mechanical constraints

2.1.1 Minimum slenderness constraints

As previously discussed in Section 1.2.2, the TTO method has limitations due to its reliance on the truss model. Consequently, we cannot rely on the results if the model falls outside the bounds of this idealization. To better study this limit, as outlined in Section 1.2.2, we introduced a metric called bar slenderness defined as follows:

$$\lambda = \frac{\ell}{R_{\mathrm{g}}}, \tag{2.1}$$

where R_{g} represent the gyration radius of the cross-sectional area, defined as $R_{\mathrm{g}} = \sqrt{I/a_j}$. The primary objective of this section is to introduce an upper limit constraint on the cross-sectional area design variable. This constraint prevents a bar from exceeding the bounds of its idealized model, thereby enhancing the optimization process's robustness.

Remembering that for a circular cross-section $I = \pi r_j^4/4$, we can write

$$R_{\mathrm{g},j} = \frac{r_j}{2}. \tag{2.2}$$

The minimum slenderness limit constraints are then stated as:

$$a_j \leq \frac{4\pi\ell_j^2}{\lambda_{\max}}, \quad \forall j \in [1, \dots, N_{\mathrm{el}}] \tag{g_{slend}}$$

for a fixed $\lambda_{\max}$. In this thesis we set $\lambda_{\max} = 15$.

2.1.2 Local and topological buckling constraints

Adding local buckling constraints to the optimization formulation is fundamental, as ultralight truss structures are often dominated by this mode of failure [50]. By imposing local buckling constraints over a TTO problem (where the lower bound for the members' cross-sectional areas is 0), the optimization domain becomes disjointed [56]. The solution is to be searched inside a degenerate space of the design space of the optimization, known in the literature as singular optimum [57]. Stolpe [58] showed how using the SAND formulation with local buckling and kinematic compatibility constraints, it is possible to find well-optimized structures without the use of relaxation techniques. The authors, however, point out how the solution is still very sensitive to the initialization point of the Non-Linear Programming (NLP) formulation. The local buckling constraints g_{buck} are stated using Euler's critical load formula as:

$$q_j + \frac{s_j a_j^2}{\ell_j^2} \geq 0 \quad \forall j \in [1, \dots, N_{\text{el}}], \tag{g_{buck}}$$

where s_j is a parameter dependent on the member material and section topology as follows:

$$s_j = \pi^2 E \beta_j. \tag{2.3}$$

$\beta_j = I_j / a_j^2$ is a positive constant dependent on the moment of inertia and the section of the j-th bar, and E is Young's modulus of the material. Assuming that the shape of the cross-section is identical over the whole structure and is independent of a, it follows that $\beta_j = \beta$ and $s_j = s,\ \forall j \in [1, \dots, N_{\text{el}}]$.

Direct application of the local buckling constraint g_{buck} in the optimization formulation tends to create "chains" of unstable compressive members [59–61]. This problem is known in the literature as topological buckling [62], as the definition of the compressive chains is a function of the topology of the structure, and is one of the elements of the nodal stability of the structure. Additional forms of structure instability, such as global buckling [63, 64] or the use of lateral perturbing forces to obtain nodal stability [65, 66] have been studied in the literature. However, since they are beyond the scope of this work, they will not be discussed further.

To illustrate the topological buckling phenomenon, we consider the case shown in Fig. 2.1a. It consists of a ground structure with $M = 3$ nodes and $N_{\text{el}} = 2$ bars with length $\ell_1 = \ell_2 = \ell$, and a compressive load of magnitude F applied at the right-hand side node. For this trivial structure, we can state that $q_1 = q_2 = F$ and thus $a_1 = a_2 = a$. We suppose here that the allowables of the material are such that the local buckling (and not the stress) is the most limiting failure criterion

50. Sigmund et al. (2016), 'On the (non-)optimality of Michell structures'
56. Cheng (1995), 'Some aspects of truss topology optimization'
57. Guo et al. (2001), 'A new approach for the solution of singular optima in truss topology optimization with stress and local buckling constraints'
58. Stolpe et al. (2003), 'A note on stress-constrained truss topology optimization'
59. Bendsøe (1995), 'Optimization of Structural Topology, Shape, and Material'
60. Zhou (1996), 'Difficulties in truss topology optimization with stress and local buckling constraints'
61. Rozvany (1996), 'Difficulties in truss topology optimization with stress, local buckling and system stability constraints'
62. Achtziger (1999), 'Local stability of trusses in the context of topology optimization Part I'
63. Ben-Tal et al. (2000), 'Optimal Design of Trusses Under a Nonconvex Global Buckling Constraint'
64. Kočvara (2002), 'On the modelling and solving of the truss design problem with global stability constraints'
65. Tyas et al. (2006), 'Practical plastic layout optimization of trusses incorporating stability considerations'
66. Mela (2014), 'Resolving issues with member buckling in truss topology optimization using a mixed variable approach'

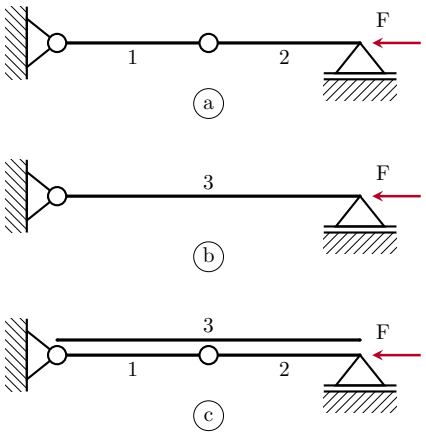

Figure 2.1: The three ground structures loaded in compression are used to highlight the topological buckling problem in TTO. (a) Two-bar ground structure loaded in compression; (b) single bar ground structure; (c) overlap of the a and b ground structures.

for the bars. Assuming that the shape of the section is equal, the local buckling constraints are written as:

$$q_j \geq -\frac{sa^2}{\ell^2}, \quad j \in [1,2]. \tag{2.4}$$

However, the structure is unstable because the vertical force equilibrium equation evaluated on the central hinge is satisfied only in an ideal case where no structural imperfections are taken into account.

If the hinge between bars 1 and 2 is deleted, we obtain the structure pictured in Fig. 2.1b with $\ell_3 = 2\ell$. The local buckling constraints for bar 3 are thus:

$$q_3 \geq -\frac{sa_3^2}{(2\ell)^2}. \tag{2.5}$$

Combining Equations 2.4,, 2.5 and observing that $q_1 = q_2 = q_3 = F$, it is now trivial to demonstrate that $a_3 = 2a$. Constraint 2.5 leads, then, to more voluminous structures compared to constraint 2.4. For that reason, even if we consider the ground structure given in Fig. 2.1c composed by the superposition of the ground structures in Fig. 2.1a and Fig. 2.1b, the optimization with a uniform initialization tends to converge to the solution $\boldsymbol{a}^* = [a, a, 0]$, unstable but lighter than the physical solution $\boldsymbol{a}_p^* = [0, 0, 2a]$.

The easiest way to get rid of the instability of the compressive chains is to post-process the optimized structure to remove the unstable hinges between the compressive bars. Doing that, the local buckling constraints are not satisfied anymore as the effective buckling length has increased. It is, then, necessary to calculate the section of the new compressive bars to comply with the newly introduced buckling constraints. As extensively shown by Achtziger [67], this post-processing phase leads to structures that are less optimal compared to the ones we could obtain if we take into account the topological buckling in the optimization in the first place.

67. Achtziger (1999), 'Local stability of trusses in the context of topology optimization Part II'

For that reason, Achtziger proposes an update strategy to modify the

length used to evaluate the critical buckling force of g_{buck} as follows:

$$\ell_j^*(\boldsymbol{a}) := \begin{cases} \ell_j & \text{if } j \notin \mathscr{C}_{l,r}(\boldsymbol{a}) \\ \sum \ell_r \mid r \in \mathscr{C}_{l,r}(\boldsymbol{a}) & \text{otherwise,} \end{cases} \tag{2.6}$$

where r represents the r-th bar of the l-th compression chain of the structure. The topology-dependent set $\mathscr{C}_{l,r}(\boldsymbol{a})$ is defined as the set of r member indexes of the l-th buckling chain. As internal forces on buckling chains are constant, only the buckling length of the first member of the chain ($\ell_j^*(\boldsymbol{a})$ with $j \in \mathscr{C}_{l,1}(\boldsymbol{a})$) is modified. Additionally, we add the following side constraints on the other members of the l-th chain to ensure feasibility:

$$a_r \geq a_{r=1} \quad r \in \mathscr{C}_{l,r}(\boldsymbol{a}),\ \forall r \neq 1. \tag{2.7}$$

2.1.3 Kinematic compatibility constraints

To optimize test cases that result in statically indeterminate structures, such as structures loaded with multiple load cases or imposed symmetries, one needs to consider kinematic compatibility in the optimization formulation [68, 69]. Compatibility can be imposed as a nonlinear constraint in the optimization formulation [70], or can be taken into account by prestressing the initial structure [71].

68. Kirsch (1989), 'Optimal topologies of truss structures'
69. Rozvany et al. (1995), 'Layout Optimization of Structures'
70. Kirsch (1980), 'Optimal design of trusses by approximate compatibility'
71. Kirsch (1989), 'Effect of Compatibility and Prestressing on Optimized Trusses'

The kinematic compatibility constraints restrict the displacement field $\boldsymbol{U} = [U_1, \ldots, U_{N_{\text{dof}}}]^T$ in such a way that strains ε_j and internal stresses σ_j comply with Hooke's law $\sigma_j = E_j \varepsilon_j$ with $j \in [1, \ldots, N_{\text{el}}]$. Recalling that in a truss the relationship between nodal displacements and member deformations is $\boldsymbol{b}_j^T \boldsymbol{U} = \ell_j \varepsilon_j$ with $\boldsymbol{b}$ as the j-th column of the $\boldsymbol{B}$ matrix, we can formulate the kinematic compatibility constraints $\boldsymbol{g}_{\text{comp}}$ as:

$$q_j - \frac{a_j E_j}{\ell_j} \boldsymbol{b}_j^T \boldsymbol{U} = 0 \quad \forall j \in [1, \ldots, N_{\text{el}}]. \tag{$\boldsymbol{g}_{\text{comp}}$}$$

Kinematic compatibility constraints are non-linear as the design variable $\boldsymbol{q}$ is dependent on $\boldsymbol{a}$ and $\boldsymbol{U}$.

2.2 Optimization formulation and solving strategy

In this section, we propose an innovative TTO formulation developed specifically to minimize the mass of 3D ultralight truss structures, taking into account maximum stress, topological buckling, and kinematic compatibility constraints. Combining Formulation $\mathbb{P}_0$ with Equations g_{buck},, 2.6, 2.7, and $\boldsymbol{g}_{\text{comp}}$ the Formulation $\mathbb{P}_1$ is stated in terms of members' cross-sectional area $\boldsymbol{a}$, member forces $\boldsymbol{q}$ and nodal

displacements $\boldsymbol{U}$ as follows:

$$
\begin{aligned}
\min_{\substack{\boldsymbol{a},\boldsymbol{q}^0,\dots,\boldsymbol{q}^{N_p},\\ \boldsymbol{U}^0,\dots,\boldsymbol{U}^{N_p}}} \quad & V = \boldsymbol{\ell}^T \boldsymbol{a} \\
\text{s.t.} \quad & \boldsymbol{B}\boldsymbol{q}^p = \boldsymbol{f}^p && \forall p \in [0,\dots,N_p] \\
& \boldsymbol{q}^p = \frac{\boldsymbol{a}E}{\boldsymbol{\ell}} \boldsymbol{b}^T \boldsymbol{U}^p && \forall p \in [0,\dots,N_p] \\
& \boldsymbol{q}^p \geq -\frac{s\boldsymbol{a}^2}{\boldsymbol{\ell}^{*2}} && \forall p \in [0,\dots,N_p] \\
& -\sigma_c \boldsymbol{a} \leq \boldsymbol{q}^p \leq \sigma_t \boldsymbol{a} && \forall p \in [0,\dots,N_p] \\
& a_r \geq a_{r=1} && r \in \mathscr{C}_{l,r}(\boldsymbol{a}) \\
& \boldsymbol{a} \geq 0.
\end{aligned}
\tag{$\mathbb{P}_1$}
$$

The formulation has been extended to multiple load cases given by N_p external loads vector $\boldsymbol{f}^0,\dots,\boldsymbol{f}^{N_p}$ and the resulting internal forces $\boldsymbol{q} = [\boldsymbol{q}^0,\dots,\boldsymbol{q}^{N_p}]$ and displacements $\boldsymbol{U} = [\boldsymbol{U}^0,\dots,\boldsymbol{U}^{N_p}]$. This proposed formulation expands the multiple load cases formulation of Achtziger [62] with kinematic compatibility constraints, permitting the correct evaluation of the mechanical state of statically indeterminate structures.

62. Achtziger (1999), 'Local stability of trusses in the context of topology optimization Part I'

The formulation follows the SAND approach [5], where, in addition to the members' cross-sectional area $\boldsymbol{a}$, the member forces $\boldsymbol{q}$ and the structure displacements $\boldsymbol{U}$ are used as state variables. One of the advantages of SAND approach is that the state variables are independent of each other and, thus, the sensitivity calculation of the constraints functions is usually simpler and leads to sparse partial derivatives. Additionally, compared to NAND formulations, the problem stays well-posed even if the cross-sectional area goes to 0. As the linear system $\boldsymbol{K}\boldsymbol{U} = \boldsymbol{f}$ is never explicitly solved during the optimization, it is not necessary to impose a lower bound on the members' cross-sectional area $\boldsymbol{a}$ to avoid a singular stiffness matrix. The last important advantage is that thanks to $\boldsymbol{U}$ being design variables, it is trivial to add bound constraints on the nodal displacements of the structure if needed.

5. Sankaranarayanan et al. (1994), 'Truss topology optimization with simultaneous analysis and design'

2.2.1 Optimization strategy

Formulation $\mathbb{P}_1$ presents multiple constraints and design variables for every physical bar of the ground structure. The quantity of constraints creates a highly non-linear design space and it proved to be hard for the optimizer to bring to zero the value of the cross-sectional areas. If a NLP optimizer is directly used on Formulation $\mathbb{P}_1$, the resulting structure will be composed of a multitude of intersecting bars. The optimizer is, thus, working like it is performing sizing optimization instead of topology optimization.

Inspired by the early works by Reinschmidt [72], we propose a novel

72. Reinschmidt et al. (1974), 'Applications of linear programming in structural layout and optimization'

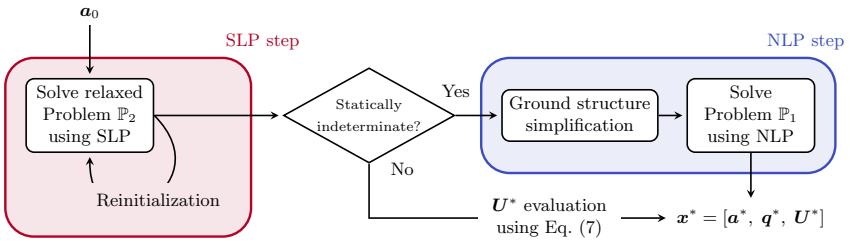

Figure 2.2: Flowchart of the two-step optimization strategy used to solve Problem $\mathbb{P}_1$.

two-step optimization strategy in which a first optimization solving a relaxed formulation is used to find a good starting point for the second optimization, solving the full Formulation $\mathbb{P}_1$. Doing that way, the first optimization explores extensively the relaxed and more regular design space and finds simpler structures, while the second optimization refines the solution imposing additional mechanical constraints. The complete solving strategy is graphically presented in Fig. 2.2.

In the first step, Problem $\mathbb{P}_1$ is relaxed: kinematic compatibility constraints are omitted. We call this relaxed Problem $\mathbb{P}_2$. Problem $\mathbb{P}_2$ is solved using a Sequential Linear Programming (SLP) method by iteratively linearizing the local buckling constraints. A heuristic strategy called Reinitialization is iteratively used to reduce the influence of the starting point $\boldsymbol{a}_0$. The resulting structure described by the design variables vector $\tilde{\boldsymbol{x}}^*$ is then post-processed, removing the members whose optimized area is below a fixed cross-sectional area threshold value. The structures generated by solving the relaxed Problem $\mathbb{P}_2$ proved to be simpler i.e. fewer active members compared to directly solving $\mathbb{P}_1$ with a NLP optimizer. If the solution is not statically indeterminate the optimization is completed as the kinematic compatibility constraints g_{comp} are automatically satisfied and, thus, used to evaluate the optimal displacements.

Otherwise, a second step is needed. Firstly, the ground structure of the problem is simplified, removing all the members that do not appear in the solution of the relaxed Problem $\mathbb{P}_2$ i.e. avoiding the reintroduction of members discarded by the SLP step. Then, the kinematic compatibility and the exact local buckling constraints are restored, and Problem $\mathbb{P}_1$ is solved in its original form on the simplified ground structure using a NLP optimizer. The initial values for the cross-sectional areas are the solution $\tilde{\boldsymbol{x}}^*$ of Problem $\mathbb{P}_2$.

2.2.2 First step: SLP optimization

The first step of the proposed optimization strategy is here described in detail. The relaxed Problem $\mathbb{P}_2$ obtained by omitting g_{comp} and the

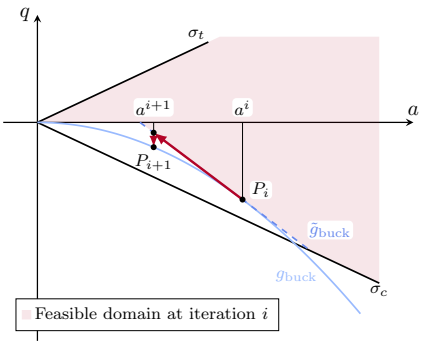

Figure 2.3: magari mettila nel margin Linearization of the local buckling constraints for a single bar.

displacements $\boldsymbol{U}$ in Formulation $\mathbb{P}_1$ is stated as:

$$
\begin{aligned}
\min_{\boldsymbol{a},\boldsymbol{q}^0,\dots,\boldsymbol{q}^P} \quad & V = \boldsymbol{\ell}^T \boldsymbol{a} & \\
\text{s.t.} \quad & \boldsymbol{B}\boldsymbol{q}^p = \boldsymbol{f}^p & \forall p \in [0,\dots,N_p] \\
& \boldsymbol{q}^p \geq -\frac{s\boldsymbol{a}^2}{\boldsymbol{\ell}^{*2}} & \forall p \in [0,\dots,N_p] \\
& -\sigma_c \boldsymbol{a} \leq \boldsymbol{q}^p \leq \sigma_t \boldsymbol{a} & \forall p \in [0,\dots,N_p] \\
& a_r \geq a_{r=1} & r \in \mathcal{C}_{l,r}(\boldsymbol{a}) \\
& \boldsymbol{a} \geq 0. &
\end{aligned}
\tag{$\mathbb{P}_2$}
$$

Since the objective function and all of its constraints are linear, except for the buckling constraint, this problem is solved by iteratively linearizing the non-linear buckling constraints and using a SLP algorithm. Following the work of [73], the Euler's critical load is iteratively updated using a first-order Taylor expansion for every j member with cross-sectional area a_j^i at the iteration i in the neighborhood of the point $\boldsymbol{P}_i$ (see Fig. 2.3):

73. Schwarz et al. (2018), 'Efficient size and shape optimization of truss structures subject to stress and local buckling constraints using sequential linear programming'

$$
\tilde{q}_{i,j}^{\text{cr}} = q_{i,j}^{\text{cr}}(a_j^i) + (a_j^{i+1} - a_j^i) \left. \frac{\partial q_{i,j}^{\text{cr}}(a_j^i)}{\partial a} \right|_{a=a_j^i} \tag{2.8}
$$

where a_j^{i+1} represent the design variable of the SLP at the current iteration and $q_{i,j}^{\text{cr}}(a_j^i) = -s(a_j^i)^2/\ell_j^{*2}$ represents the Euler's critical load with cross-sectional area a_j^i and modified buckling length ℓ_j^*.

The linearized local buckling constraints $\tilde{\boldsymbol{g}}_{\text{buck}}$ are then stated as:

$$
q_j \geq \tilde{q}_{i,j}^{\text{cr}}, \text{ with } \tilde{q}_{i,j}^{\text{cr}} = -\frac{s a_j^i \left(2a_j^{i+1} - a_j^i\right)}{\ell_j^{*2}} \quad \forall j \in [1,\dots,N_{\text{el}}], \quad (\tilde{\boldsymbol{g}}_{\text{buck}})
$$

where superscript $\sim$ indicates linearized functions and corresponding variables.

We can now state the relaxed linearized sub-problem $\tilde{\mathbb{P}}_2$ obtained

substituting g_{buck} with $\tilde{g}_{\text{buck}}$ in Formulation $\mathbb{P}_2$:

$$
\begin{aligned}
\min_{\boldsymbol{a},\boldsymbol{q}^0,\dots,\boldsymbol{q}^p} \quad & V = \boldsymbol{\ell}^T \boldsymbol{a} & & \\
\text{s.t.} \quad & \boldsymbol{B}\boldsymbol{q}^p = \boldsymbol{f}^p & & \forall p \in [0,\dots,N_p] \\
& \boldsymbol{q}^p \geq -\frac{s\boldsymbol{a}^i\left(2\boldsymbol{a}^{i+1} - \boldsymbol{a}^i\right)}{\boldsymbol{\ell}^{*2}} & & \forall p \in [0,\dots,N_p] \qquad (\tilde{\mathbb{P}}_2) \\
& -\sigma_c \boldsymbol{a} \leq \boldsymbol{q}^p \leq \sigma_t \boldsymbol{a} & & \forall p \in [0,\dots,N_p] \\
& a_r \geq a_{r=1} & & r \in \mathscr{C}_{l,r}(\boldsymbol{a}) \\
& \boldsymbol{a} \geq 0. & &
\end{aligned}
$$

Since the objective function and all of its constraints are linear, we can approximate the solution of $\mathbb{P}_2$ by iteratively solving the sub-problem $\tilde{\mathbb{P}}_2$. At every iteration i, the vector of cross-sectional areas $\boldsymbol{a}^i$ is used to evaluate the linearization point $\boldsymbol{P}_i$ and calculate the set of linearized buckling constraints $\tilde{\boldsymbol{g}}_{\text{buck}}$ (see Fig. 2.3). The sub-problem $\tilde{\mathbb{P}}_2$ is, then, solved using a LP solver, and the updated vector of cross-sectional areas $\boldsymbol{a}^{i+1}$ is used to evaluate the set of linearized buckling constraints of the $i+1$ iteration. These steps are repeated until convergence i.e. when $\|\Delta\boldsymbol{x}\|_\infty \leq \text{tol}_{slp}$, where $\Delta\boldsymbol{x}$ represents the difference of the design variable vector $\boldsymbol{x}$ between two successive iterations. The vector $\boldsymbol{x}$ is scaled so that the difference $\Delta\boldsymbol{x}$ gives coherent results for the different physical quantities (cross-sectional areas and forces). Major details on scaling are given in Appendix.

2.2.3 Handling local minima: reinitialization strategy

2.2.4 Second step: NLP optimization

2.3 Numerical application

2.3.1 L-shaped beam

To assess the effectiveness of the proposed minimum slenderness limit, we conducted a new round of optimization on the L-shaped beam described in Section 1.2.2. Formulation $\mathbb{P}_0$ is modified adding an upper bound on the cross-sectional section based on g_{slend}. In the Fig. 2.4, we present the optimized structures obtained using this modified formulation and the stress limits σ_{L} values of 1, 0.8, 0.3, and 0.2. The first two values have already been used and the results presented in Table 1.3. They highligted the limits of Formulation $\mathbb{P}_0$ when imposing a specified slenderness limit ($\lambda < 15$). The last two values are introduced here to test how the g_{slend} constraint affect the truss topology for extreme cases.

Major focus is put on the shorter bar of the optimized structures to observe how the solution evolved. We observe a redistribution of the same load across multiple smaller bars. More bars became active because there is an upper limit on the cross-sectional area (and thus

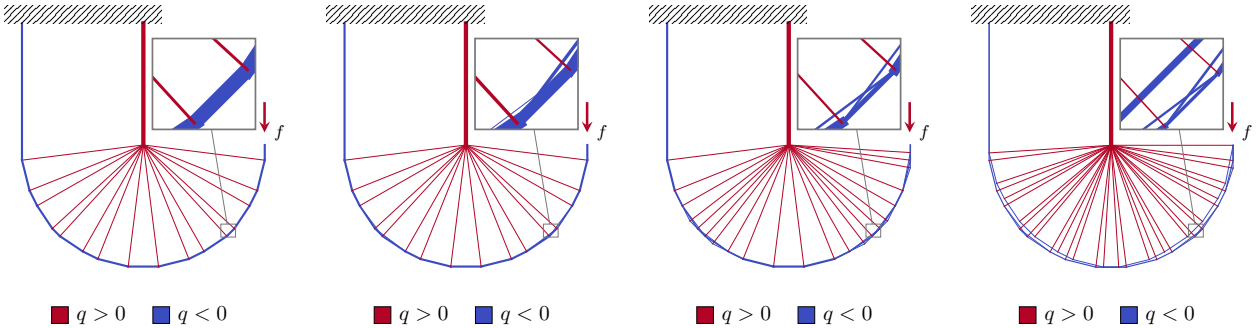

Figure 2.4: Topology of the optimized truss structures for different material admissibles $\sigma_L = 1.0, 0.8, 0.3$ and 0.2 with a minimum slenderness limit $\lambda < 15$.

Table 2.2: todo

σ_L	V_f	Min λ	$V_{f,sl}$	Min λ_{sl}	$V_{f,sl}/V_f$	$N_{el,sl}/N_{el}$	t_{sl}/t
1.0	6.21 %	15.8	6.21 %	15.8	1.0000	1.00	1.02
0.9	6.90 %	15.0	6.90 %	15.0	1.0000	1.00	1.03
0.8	7.76 %	14.1	7.76 %	15.0	1.0001	1.12	2.27
0.7	8.87 %	13.2	8.87 %	15.0	1.0001	1.12	2.21
0.6	10.35 %	12.2	10.35 %	15.0	1.0002	1.12	1.12
0.5	12.42 %	11.2	12.42 %	15.0	1.0003	1.12	1.07
0.4	–	–	15.53 %	15.0	–	–	–
0.3	–	–	20.71 %	15.0	–	–	–
0.2	–	–	31.06 %	15.0	–	–	–

the force) they can withstand. The four structures present $N_{el,sl} = 34$, 38, 56 and 79 active bars, respectively.

In Table 2.2 we compared the new designs limited in minimum slenderness (noted in the table with the 'sl' subscript) to the ones presented in Section 1.2.2 and found that the new designs meet the bar model's slenderness requirements correctly. The number of active bars increases along with the calculation time, but the volume remains nearly the same, indicating there are many solutions with similar volumes. Adding this upper bound constraint, we have extended the domain of application of the TTO. However, we must be careful because very high volumes fraction solutions can lead to too many bar intersections, resulting in structures with no physical meaning.

2.3.2 Ten-bar truss

2.3.3 2D cantilever beam

2.3.4 Simply supported 3D beam

2.3.5 Ten-bar truss with multiple load cases

2.4 Conclusion

2.5 temporary

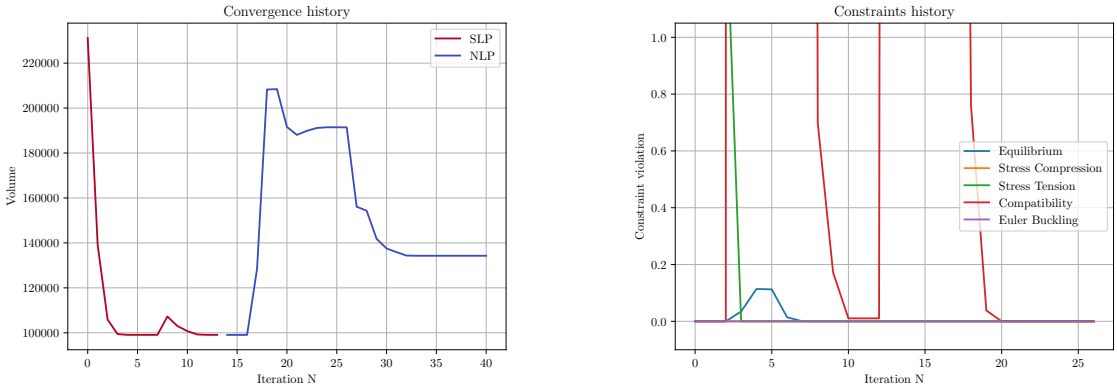

(a) **(b)**

Figure 2.5: Iteration history of the ten-bar truss with multiple load cases example solved with the 2S-1R algorithm; (a) objective function history for the SLP and NLP step (b) constraint violation for the NLP step.

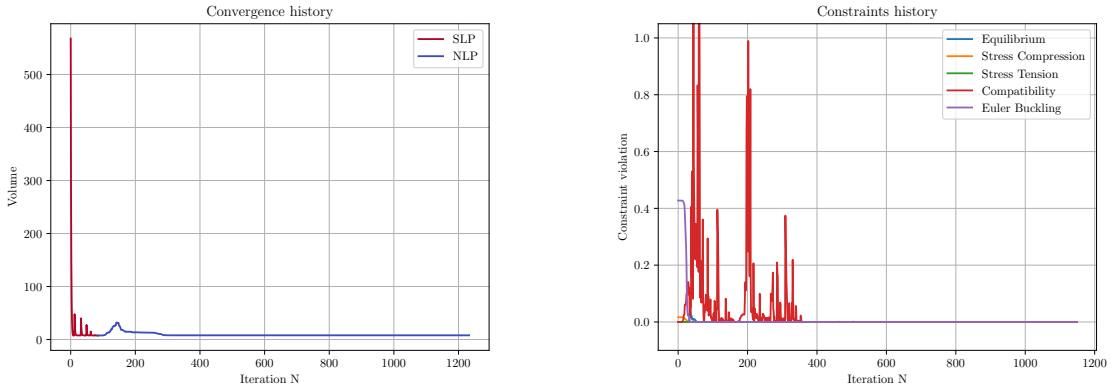

(a) **(b)**

Figure 2.6: Iteration history of the CRM-315 example solved with the 2S-5R algorithm; (a) objective function history for the SLP and NLP step (b) constraint violation for the NLP step.

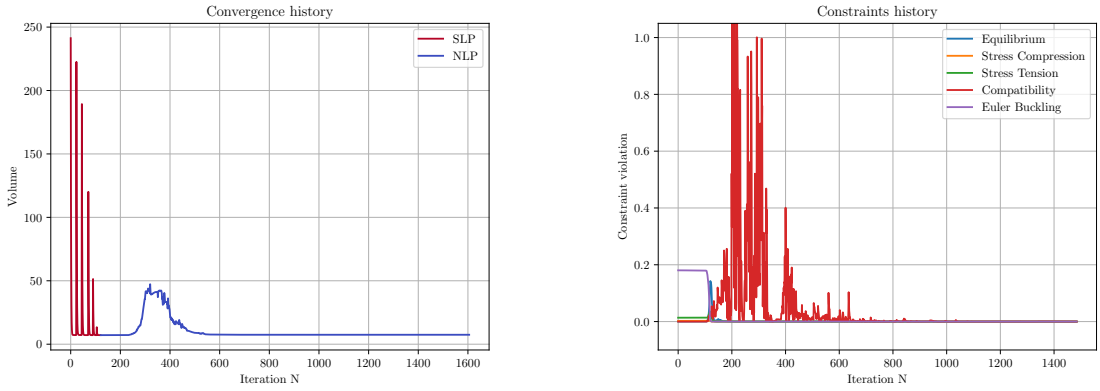

(a) **(b)**

Figure 2.7: Iteration history of the CRM-2370 example solved with the 2S-5R algorithm; (a) objective function history for the SLP and NLP step (b) constraint violation for the NLP step.

Bibliography

[1] Stragiotti, Enrico, Irisarri, François-Xavier, Julien, Cédric, and Morlier, Joseph, 'Towards manufactured lattice structures: a comparison between layout and topology optimization', *AeroBest 2021 International Conference on Multidisciplinary Design Optimization of Aerospace Systems. Book of proceedings*, Lisbon, Portugal: ECCOMAS, July 2021, pp. 229–244. cited on page 1

[2] Dorn, W. S., Gomory, Ralph E., and Greenberg, H., 'Automatic design of optimal structures', *J. Mécanique* (1964). cited on pages 1, 12, 13

[3] Chan, H. S. Y., 'Optimum structural design and linear programming', *College of Aeronautics Report Aero 175* (1964), Publisher: College of Aeronautics Cranfield. cited on pages 1, 12

[4] Hemp, W. S., 'Optimum Structures'. Clarendon Press, 1973, Google-Books-ID: cJhpAAAAMAAJ.
ISBN: 978-0-19-856110-1 cited on pages 1, 11, 12

[5] Sankaranarayanan, S., Haftka, Raphael T., and Kapania, Rakesh K., 'Truss topology optimization with simultaneous analysis and design', *AIAA Journal* 32.2 (Feb. 1994), pp. 420–424.
DOI: 10.2514/3.12000 cited on pages 1, 30

[6] Bendsøe, Martin Philip and Kikuchi, Noboru, 'Generating optimal topologies in structural design using a homogenization method', *Computer Methods in Applied Mechanics and Engineering* 71.2 (Nov. 1988), pp. 197–224.
DOI: 10.1016/0045-7825(88)90086-2 cited on pages 1, 16

[7] Bendsøe, M. P., 'Optimal shape design as a material distribution problem', *Structural optimization* 1.4 (Dec. 1989), pp. 193–202.
DOI: 10.1007/BF01650949 cited on pages 1, 3, 13, 23

[8] Sigmund, Ole, 'Materials with prescribed constitutive parameters: An inverse homogenization problem', *International Journal of Solids and Structures* 31.17 (Sept. 1994), pp. 2313–2329.
DOI: 10.1016/0020-7683(94)90154-6 cited on page 1

[9] Zhang, Weihong and Sun, Shiping, 'Scale-related topology optimization of cellular materials and structures', *International Journal for Numerical Methods in Engineering* 68.9 (2006), pp. 993–1011.
DOI: 10.1002/nme.1743 cited on page 1

[10] Sigmund, Ole, 'Manufacturing tolerant topology optimization', *Acta Mechanica Sinica* 25.2 (Apr. 2009), pp. 227–239.
DOI: 10.1007/s10409-009-0240-z cited on page 1

[11] Brackett, D, Ashcroft, I, and Hague, R, 'Topology Optimization for Additive Manufacturing' (2011), p. 15.
DOI: 10.26153/tsw/15300 cited on page 1

cited on page 2 [12] Tortorelli, D. A. and Michaleris, P., 'Design sensitivity analysis: Overview and review', *Inverse Problems in Engineering* 1.1 (Oct. 1994), pp. 71–105.
DOI: 10.1080/174159794088027573

cited on pages 2, 10 [13] Martins, J.R.R.A. and Ning, A., 'Engineering Design Optimization'. Cambridge University Press, 2021.
ISBN: 978-1-108-83341-7

cited on pages 2, 10, 13 [14] Bendsøe, Martin P. and Sigmund, Ole, 'Topology Optimization'. Berlin, Heidelberg: Springer Berlin Heidelberg, 2004.
ISBN: 978-3-642-07698-5 978-3-662-05086-6

cited on pages 3, 4 [15] Wang, Fengwen, Lazarov, Boyan Stefanov, and Sigmund, Ole, 'On projection methods, convergence and robust formulations in topology optimization', *Structural and Multidisciplinary Optimization* 43.6 (June 2011), pp. 767–784.
DOI: 10.1007/s00158-010-0602-y

cited on page 3 [16] Bendsøe, M. P. and Sigmund, O., 'Material interpolation schemes in topology optimization', *Archive of Applied Mechanics* 69.9 (Nov. 1999), pp. 635–654.
DOI: 10.1007/s004190050248

cited on page 3 [17] Hashin, Z. and Shtrikman, S., 'A variational approach to the theory of the elastic behaviour of multiphase materials', *Journal of the Mechanics and Physics of Solids* 11.2 (Mar. 1963), pp. 127–140.
DOI: 10.1016/0022-5096(63)90060-7

cited on page 3 [18] Díaz, A. and Sigmund, O., 'Checkerboard patterns in layout optimization', *Structural optimization* 10.1 (Aug. 1995), pp. 40–45.
DOI: 10.1007/BF01743693

cited on page 4 [19] Sigmund, Ole, 'Design of Material Structures using Topology Optimization', PhD thesis, Technical University of Denmark, DK-2800 Lyngby, 1994.

cited on page 4 [20] Sigmund, Ole, 'On the Design of Compliant Mechanisms Using Topology Optimization', *Mechanics of Structures and Machines* 25.4 (Jan. 1997), pp. 493–524.
DOI: 10.1080/08905459708945415

cited on pages 4, 16 [21] Sigmund, Ole, 'Morphology-based black and white filters for topology optimization', *Structural and Multidisciplinary Optimization* 33.4 (Apr. 2007), pp. 401–424.
DOI: 10.1007/s00158-006-0087-x

cited on pages 4, 15 [22] Ferrari, Federico and Sigmund, Ole, 'A new generation 99 line Matlab code for compliance topology optimization and its extension to 3D', *Structural and Multidisciplinary Optimization* 62.4 (Oct. 2020), pp. 2211–2228.
DOI: 10.1007/s00158-020-02629-w

[23] Achtziger, Wolfgang and Kanzow, Christian, 'Mathematical programs with vanishing constraints: optimality conditions and constraint qualifications', *Mathematical Programming* 114.1 (July 2008), pp. 69–99. DOI: 10.1007/s10107-006-0083-3 cited on page 5

[24] Cheng, Gengdong and Jiang, Zheng, 'Study on Topology Optimization with Stress Constraints', *Engineering Optimization* 20.2 (Nov. 1992), pp. 129–148. DOI: 10.1080/03052159208941276 cited on page 5

[25] Duysinx, P. and Bendsøe, M. P., 'Topology optimization of continuum structures with local stress constraints', *International Journal for Numerical Methods in Engineering* 43.8 (1998), pp. 1453–1478. DOI: 10.1002/(SICI)1097-0207(19981230)43:8<1453::AID-NME480>3.0.CO;2-2 cited on pages 6, 14

[26] Le, Chau, Norato, Julian, Bruns, Tyler, Ha, Christopher, and Tortorelli, Daniel, 'Stress-based topology optimization for continua', *Structural and Multidisciplinary Optimization* 41.4 (Apr. 2010), pp. 605–620. DOI: 10.1007/s00158-009-0440-y cited on pages 6, 7, 14

[27] Verbart, Alexander, Langelaar, Matthijs, and Keulen, Fred van, 'A unified aggregation and relaxation approach for stress-constrained topology optimization', *Structural and Multidisciplinary Optimization* 55.2 (Feb. 2017), pp. 663–679. DOI: 10.1007/s00158-016-1524-0 cited on pages 6, 7, 15

[28] Holmberg, Erik, Torstenfelt, Bo, and Klarbring, Anders, 'Stress constrained topology optimization', *Structural and Multidisciplinary Optimization* 48.1 (2013), pp. 33–47. DOI: 10.1007/s00158-012-0880-7 cited on page 7

[29] Silva, Gustavo Assis da, Beck, André Teófilo, and Sigmund, Ole, 'Stress-constrained topology optimization considering uniform manufacturing uncertainties', *Computer Methods in Applied Mechanics and Engineering* 344 (Feb. 2019), pp. 512–537. DOI: 10.1016/j.cma.2018.10.020 cited on page 7

[30] Rozvany, G.I.N., 'On design-dependent constraints and singular topologies', *Structural and Multidisciplinary Optimization* 21.2 (Apr. 2001), pp. 164–172. DOI: 10.1007/s001580050181 cited on page 7

[31] Stolpe, Mathias, 'On Models and Methods for Global Optimization of Structural Topology', Publisher: Matematik, PhD thesis, 2003. cited on page 7

[32] Sved, G. and Ginos, Z., 'Structural optimization under multiple loading', *International Journal of Mechanical Sciences* 10.10 (Oct. 1968), pp. 803–805. DOI: 10.1016/0020-7403(68)90021-0 cited on page 7

cited on page 7 [33] Cheng, G. D. and Guo, X., 'ε-relaxed approach in structural topology optimization', *Structural optimization* 13.4 (June 1997), pp. 258–266.
DOI: 10.1007/BF01197454

cited on page 7 [34] Silva, Gustavo Assis da, Aage, Niels, Beck, André Teófilo, and Sigmund, Ole, 'Local versus global stress constraint strategies in topology optimization: A comparative study', *International Journal for Numerical Methods in Engineering* 122.21 (2021), pp. 6003–6036.
DOI: 10.1002/nme.6781

cited on page 8 [35] Kreisselmeier, G. and Steinhauser, R., 'Systematic Control Design by Optimizing a Vector Performance Index', *IFAC Proceedings Volumes*, IFAC Symposium on computer Aided Design of Control Systems, Zurich, Switzerland, 29-31 August 12.7 (Sept. 1979), pp. 113–117.
DOI: 10.1016/S1474-6670(17)65584-8

cited on page 11 [36] Maxwell, J. Clerk, 'I.—On Reciprocal Figures, Frames, and Diagrams of Forces', *Earth and Environmental Science Transactions of The Royal Society of Edinburgh* 26.1 (1870), Publisher: Royal Society of Edinburgh Scotland Foundation, pp. 1–40.
DOI: 10.1017/S0080456800026351

cited on pages 11, 13 [37] Michell, A. G. M., 'The limits of economy of material in frame-structures', *The London, Edinburgh, and Dublin Philosophical Magazine and Journal of Science* 8.47 (Nov. 1904), pp. 589–597.
DOI: 10.1080/14786440409463229

cited on pages 12, 13 [38] Gilbert, Matthew and Tyas, Andrew, 'Layout optimization of large-scale pin-jointed frames', *Engineering Computations* 20.8 (Dec. 2003), pp. 1044–1064.
DOI: 10.1108/02644400310503017

cited on page 12 [39] Pedersen, Pauli, 'Optimal Joint Positions for Space Trusses', *Journal of the Structural Division* 99.12 (Dec. 1973), Publisher: American Society of Civil Engineers, pp. 2459–2476.
DOI: 10.1061/JSDEAG.0003669

cited on page 12 [40] Achtziger, Wolfgang, 'On simultaneous optimization of truss geometry and topology', *Structural and Multidisciplinary Optimization* 33.4 (Apr. 2007), pp. 285–304.
DOI: 10.1007/s00158-006-0092-0

cited on page 12 [41] Descamps, Benoît and Filomeno Coelho, Rajan, 'A lower-bound formulation for the geometry and topology optimization of truss structures under multiple loading', *Structural and Multidisciplinary Optimization* 48.1 (July 2013), pp. 49–58.
DOI: 10.1007/s00158-012-0876-3

cited on page 12 [42] He, L. and Gilbert, M., 'Rationalization of trusses generated via layout optimization', *Structural and Multidisciplinary Optimization* 52.4 (Oct. 2015), pp. 677–694.

DOI: 10.1007/s00158-015-1260-x

[43] Lu, Hongjia and Xie, Yi Min, 'Reducing the number of different members in truss layout optimization', *Structural and Multidisciplinary Optimization* 66.3 (Feb. 2023), p. 52. DOI: 10.1007/s00158-023-03514-y cited on page 12

[44] Parkes, E.W., 'Joints in optimum frameworks', *International Journal of Solids and Structures* 11.9 (Sept. 1975), pp. 1017–1022. DOI: 10.1016/0020-7683(75)90044-X cited on page 13

[45] Watts, Seth, Arrighi, William, Kudo, Jun, Tortorelli, Daniel A., and White, Daniel A., 'Simple, accurate surrogate models of the elastic response of three-dimensional open truss micro-architectures with applications to multiscale topology design', *Structural and Multidisciplinary Optimization* 60.5 (Nov. 2019), pp. 1887–1920. DOI: 10.1007/s00158-019-02297-5 cited on page 13

[46] Svanberg, Krister, 'The method of moving asymptotes—a new method for structural optimization', *International Journal for Numerical Methods in Engineering* 24.2 (1987), pp. 359–373. DOI: https://doi.org/10.1002/nme.1620240207 cited on page 15

[47] Johnson, Steven G., 'The NLopt nonlinear-optimization package', https://github.com/stevengj/nlopt, 2007. cited on page 15

[48] Diamond, Steven and Boyd, Stephen, 'CVXPY: A Python-Embedded Modeling Language for Convex Optimization', 2016. cited on page 15

[49] Domahidi, Alexander, Chu, Eric, and Boyd, Stephen, 'ECOS: An SOCP solver for embedded systems', *2013 European Control Conference (ECC)*, Zurich: IEEE, July 2013, pp. 3071–3076, ISBN: 978-3-033-03962-9. DOI: 10.23919/ECC.2013.6669541 cited on page 15

[50] Sigmund, Ole, Aage, Niels, and Andreassen, Erik, 'On the (non-)optimality of Michell structures', *Structural and Multidisciplinary Optimization* 54.2 (Aug. 2016), pp. 361–373. DOI: 10.1007/s00158-016-1420-7 cited on pages 16, 23, 27

[51] Bruggi, Matteo and Duysinx, Pierre, 'Topology optimization for minimum weight with compliance and stress constraints', *Structural and Multidisciplinary Optimization* 46.3 (Sept. 2012), pp. 369–384. DOI: 10.1007/s00158-012-0759-7 cited on page 17

[52] París, J., Navarrina, F., Colominas, I., and Casteleiro, M., 'Block aggregation of stress constraints in topology optimization of structures', *Advances in Engineering Software*, Advances in optimum engineering design 41.3 (Mar. 2010), pp. 433–441. DOI: 10.1016/j.advengsoft.2009.03.006 cited on page 17

cited on page 17

[53] Norato, Julián A., Smith, Hollis A., Deaton, Joshua D., and Kolonay, Raymond M., 'A maximum-rectifier-function approach to stress-constrained topology optimization', *Structural and Multidisciplinary Optimization* 65.10 (Sept. 2022), p. 286.
DOI: 10.1007/s00158-022-03357-z

cited on page 19

[54] Lewiński, T., Zhou, M., and Rozvany, G. I. N., 'Extended exact solutions for least-weight truss layouts—Part I: Cantilever with a horizontal axis of symmetry', *International Journal of Mechanical Sciences* 36.5 (1994), pp. 375–398.
DOI: 10.1016/0020-7403(94)90043-4

cited on page 22

[55] Munro, Dirk and Groenwold, Albert, 'Local stress-constrained and slope-constrained SAND topology optimisation', *International Journal for Numerical Methods in Engineering* 110.5 (May 2017), pp. 420–439.
DOI: 10.1002/nme.5360

cited on page 27

[56] Cheng, G., 'Some aspects of truss topology optimization', *Structural Optimization* 10.3-4 (Dec. 1995), pp. 173–179.
DOI: 10.1007/BF01742589

cited on page 27

[57] Guo, X., Cheng, G., and Yamazaki, K., 'A new approach for the solution of singular optima in truss topology optimization with stress and local buckling constraints', *Structural and Multidisciplinary Optimization* 22.5 (Dec. 2001), pp. 364–373.
DOI: 10.1007/s00158-001-0156-0

cited on page 27

[58] Stolpe, M. and Svanberg, K., 'A note on stress-constrained truss topology optimization', *Structural and Multidisciplinary Optimization* 25.1 (Mar. 2003), pp. 62–64.
DOI: 10.1007/s00158-002-0273-4

cited on page 27

[59] Bendsøe, Martin P., 'Optimization of Structural Topology, Shape, and Material'. Berlin, Heidelberg: Springer Berlin Heidelberg, 1995.
ISBN: 978-3-662-03117-9 978-3-662-03115-5

cited on page 27

[60] Zhou, M., 'Difficulties in truss topology optimization with stress and local buckling constraints', *Structural optimization* 11.2 (Apr. 1996), pp. 134–136.
DOI: 10.1007/BF01376857

cited on page 27

[61] Rozvany, G. I. N., 'Difficulties in truss topology optimization with stress, local buckling and system stability constraints', *Structural optimization* 11.3 (June 1996), pp. 213–217.
DOI: 10.1007/BF01197036

cited on pages 27, 30

[62] Achtziger, W., 'Local stability of trusses in the context of topology optimization Part I: Exact modelling', *Structural Optimization* 17.4 (Dec. 1999), pp. 235–246.
DOI: 10.1007/BF01206999

[63] Ben-Tal, Aharon, Jarre, Florian, Kočvara, Michal, Nemirovski, Arkadi, and Zowe, Jochem, 'Optimal Design of Trusses Under a Nonconvex Global Buckling Constraint', *Optimization and Engineering* 1.2 (July 2000), pp. 189–213. DOI: 10.1023/A:1010091831812 cited on page 27

[64] Kočvara, M., 'On the modelling and solving of the truss design problem with global stability constraints', *Structural and Multidisciplinary Optimization* 23.3 (Apr. 2002), pp. 189–203. DOI: 10.1007/s00158-002-0177-3 cited on page 27

[65] Tyas, A., Gilbert, M., and Pritchard, T., 'Practical plastic layout optimization of trusses incorporating stability considerations', *Computers & Structures* 84.3 (Jan. 2006), pp. 115–126. DOI: 10.1016/j.compstruc.2005.09.032 cited on page 27

[66] Mela, Kristo, 'Resolving issues with member buckling in truss topology optimization using a mixed variable approach', *Structural and Multidisciplinary Optimization* 50.6 (Dec. 2014), pp. 1037–1049. DOI: 10.1007/s00158-014-1095-x cited on page 27

[67] Achtziger, W., 'Local stability of trusses in the context of topology optimization Part II: A numerical approach', *Structural optimization* 17.4 (Dec. 1999), pp. 247–258. DOI: 10.1007/BF01207000 cited on page 28

[68] Kirsch, Uri, 'Optimal topologies of truss structures', *Computer Methods in Applied Mechanics and Engineering* 72.1 (Jan. 1989), pp. 15–28. DOI: 10.1016/0045-7825(89)90119-9 cited on page 29

[69] Rozvany, G. I. N., Bendsøe, M. P., and Kirsch, U., 'Layout Optimization of Structures', *Applied Mechanics Reviews* 48.2 (Feb. 1995), pp. 41–119. DOI: 10.1115/1.3005097 cited on page 29

[70] Kirsch, Uri, 'Optimal design of trusses by approximate compatibility', *Computers & Structures* 12.1 (July 1980), pp. 93–98. DOI: 10.1016/0045-7949(80)90097-8 cited on page 29

[71] Kirsch, Uri, 'Effect of Compatibility and Prestressing on Optimized Trusses', *Journal of Structural Engineering* 115.3 (Mar. 1989), pp. 724–737. DOI: 10.1061/(ASCE)0733-9445(1989)115:3(724) cited on page 29

[72] Reinschmidt, Kenneth F. and Russell, Alan D., 'Applications of linear programming in structural layout and optimization', *Computers & Structures* 4.4 (Aug. 1974), pp. 855–869. DOI: 10.1016/0045-7949(74)90049-2 cited on page 30

cited on page 32

[73] Schwarz, Jonas, Chen, Tian, Shea, Kristina, and Stanković, Tino, 'Efficient size and shape optimization of truss structures subject to stress and local buckling constraints using sequential linear programming', *Structural and Multidisciplinary Optimization* 58.1 (July 2018), pp. 171–184.
DOI: 10.1007/s00158-017-1885-z